FERRITIC-MARTENSITIC STEEL SUBJECTED TO EQUAL CHANNEL ANGULAR EXTRUSION

A Thesis

by

DAVID CHRISTOPHER FOLEY

Submitted to the Office of Graduate Studies of
Texas A&M University
in partial fulfillment of the requirements for the degree of

MASTER OF SCIENCE

December 2007

Major Subject: Mechanical Engineering

FERRITIC-MARTENSITIC STEEL SUBJECTED TO EQUAL CHANNEL ANGULAR EXTRUSION

A Thesis

by

DAVID CHRISTOPHER FOLEY

Submitted to the Office of Graduate Studies of
Texas A&M University
in partial fulfillment of the requirements for the degree of

MASTER OF SCIENCE

Approved by:

Chair of Committee,	K. Ted Hartwig
Committee Members,	Xinghang Zhang
	Amy Epps Martin
Head of Department,	Dennis L. O'Neal

December 2007

Major Subject: Mechanical Engineering

ABSTRACT

Ferritic-Martensitic Steel Subjected to Equal Channel Angular Extrusion.

(December 2007)

David Christopher Foley, B.S., Trinity University

Chair of Advisory Committee: Dr. K. Ted Hartwig

Modified 9Cr-1Mo ferritic-martensitic steel (T91) has been extensively investigated as a structural material for GenIV nuclear reactors and Accelerator Driven Transmutation systems. One attractive characteristic of this steel in these applications is its superior radiation damage tolerance in comparison to typical austenitic stainless steels such as 316L. In some GenIV applications, it also has a significantly higher corrosion resistance. Further improvement of both is necessary if GenIV designs are to become commercially viable. Other work has shown an improvement in radiation damage tolerance via cold rolling or sputtering nanoscale multilayered films. Additionally, corrosion resistance can be improved by homogenizing the microstructure. Further, these changes can improve the strength of the material. However, there has been no fabrication of bulk ultra fine grain ferritic-martensitic steel candidates that might offer these avenues of improvement. This work demonstrates the refinement and homogenization of T91 by Equal Channel Angular Extrusion (ECAE) and heat treatment. Processing temperature and strain level were varied to produce multiple levels of refinement. Materials were characterized by microhardness, tensile testing, x-ray diffraction and transmission electron microscopy.

An ultra-fine, highly misoriented and homogeneous microstructure was achieved in the material. Refinement was demonstrated both in ferritic and ferritic-martensitic compositions of the steel. Microhardness increased by as much as 70% and ultimate tensile strength by 80%. More significantly, tensile strength was improved by 40% without decreasing ductility.

DEDICATION

To the two people outside my committee who skim through this thesis: you have gained my knowledge without consuming my brain, for which I am grateful.

ACKNOWLEDGEMENTS

I would like to thank Dr. K. Ted Hartwig and Dr. Xinghang Zhang for their guidance and support throughout the process of this research. Thanks to Dr. Amy Epps Martin for ensuring that this thesis was up to par. The Department of Energy's Nuclear Research Initiative funded the project, for which I am grateful. Thanks to Peter Hoseman and Stuart Malloy at Los Alamos National Lab for collaboration and materials throughout the project. Thanks go to Robert Barber and Doug Krebbs. Their mechanical skill and knowledge prevented many problems and helped solve many more.

I am thankful to my friends and colleagues who gave their time to help me learn procedures, examine samples, and survive graduate school. Suveen Mathaudhu and Jae-Taek Im acted as student mentors throughout the work. An incomplete list of others follows: Thanks to Osman Anderoglu, Nan Li and Engang Fu for microscopy. Thanks to Ersin Karaca and Ji Ma for tensile testing. Thanks to Dr. Haiyan Wang and Rick Littleton for TEM preparation equipment training. Thanks to Dr. Michael Pendleton, Dr. Andreas Holzenburg, and the rest of the MiC staff for SEM support. Special thanks to Jennifer Taylor and all of my friends for understanding my inexplicable decision to keep going to school. I will lay partial blame for this at the feet of Dr. Peter Kelly-Zion because of the love of research that he helped to instill in me.

Finally and crucially, thanks to my mother and father for their complete and continued support. I would not have made it here without you.

TABLE OF CONTENTS

CHAPTER Page

LIST OF FIGURES

FIGURE Page

FIGURE Page

LIST OF TABLES

CHAPTER I
INTRODUCTION

The primary objective of this project is to refine and homogenize the microstructure of modified 9Cr-1Mo steel via Severe Plastic Deformation using Equal Channel Angular Extrusion. The mechanical properties and thermal stability of the steel must be investigated to determine if the processed material might be suitable for future applications proposed by the nuclear power community.

Material

Ferritic-martensitic stainless steels are robust materials with good corrosion resistance thanks to the thin oxide layer formed by chromium. Their toughness and formability lend them to applications from automotive body trim to cutlery. One specialized alloy in this group is T91, also known as modified 9Cr-1Mo steel. It is intended to resist high temperature creep and corrosion under the high pressures involved in power generation. T91 and other Cr-Mo steels have been comprehensively investigated in recent years in order to improve their performance in current applications as well as to determine their suitability for next generation nuclear power plants. These GenIV nuclear reactors require materials with resistance to high temperature creep, resistance to chemical attack and insensitivity to particle radiation damage. These are qualities that ferritic-martensitic steels are particularly suited for and thus they are the current reference point for GenIV materials. Refining the T91 microstructure to the

---

This thesis follows the style of Journal of Nuclear Materials.

Ultra Fine Grain level may lead to an increase in radiation tolerance over conventional T91. Additionally, it would be advantageous for many applications if T91 can gain strength through grain size refinement without drastic loss of ductility.

Radiation Damage

Particle radiation damage is a well-studied phenomenon in many materials. When a particle impacts a material at high speed it typically knocks an atom from its lattice position and then both the particle and displaced atom go on to displace more atoms, creating a damage cascade. The particle then becomes a point defect in the material. The lattice structure may recover from this impact or may have numerous point defects. As many particles impact a single crystal material, a normal distribution of defects versus surface depth will form. Other defects such as grain boundaries can influence this distribution, thus the interest in refining grain size.

One reason that T91 is being investigated as a radiation tolerant stainless steel is its Body Centered Cubic (BCC) structure. The lattice is more open than Face Centered Cubic (FCC) stainless steels and is therefore able to absorb more interstitials before swelling occurs. Dramatic swelling is caused by the formation of bubbles in the material, especially in the case of helium, which is essentially insoluble in metals [1]. When the bubbles reach a critical size they can combine to form voids, causing a loss of material thickness as sections flake off [2]. Before this extreme stage the material will become brittle. In T91 and other alloys an additional effect is radiation induced segregation, usually observed as a change in concentrations at grain boundaries. Some stainless steels and other materials also undergo phase transformation during irradiation [3]. These affects are sensitive to temperature, duration of exposure and particle energy. Thus,

identical materials subjected to the same total dose over different times may show significantly different damage. This makes truly representative data difficult to obtain when the application of interest involves decades or millennia of exposure.

Applications

Currently T91 and similar alloys are employed in fossil fuel power generation, boiling water reactors and chemical production. These systems could benefit from strengthening but do not require radiation damage tolerance. However, several future and current applications require a significant increase in radiation tolerance. Particle radiation has many sources but among the most severe short of a nuclear reaction is spallation, in which a nucleus is partially broken up by the impact of a particle, releasing neutrons at a high speed. This occurs in Accelerator Driven Transmutation, a process that changes the atomic weight of a material by accelerating protons at its nucleus. Since these ADT systems have the potential to significantly reduce the nuclear waste problem by reprocessing spent fuel, T91 and other steels are being examined as possible construction materials for such devices [4]. An additional radiation damage source is the natural decay of this waste during long-term storage. Several options are being explored for safely disposing of nuclear waste but current goals require containers capable of sealing the waste for 8-10 millennia. This is a significant challenge for materials scientists on many fronts and another possible ferritic-martensitic steel applications.

The most active area of study for T91 is for use as the reactor walls and primary coolant loop of GenIV reactors. These are conceptualized high-temperature reactors that utilize corrosive coolants that would improve the efficiency and possibly safety of nuclear power plants. If suitable materials can be developed, these reactors could even be

used for black-box power generation in countries without nuclear technology [5, 6]. T91 and similar steels are most promising for liquid lead-bismuth cooled reactors since the coolant leeches out nickel present in more common stainless steels such as 316 and 304. There are many hurdles to overcome with this corrosive high temperature system but lead-bismuth reactors have been utilized before in the USSR's Лира **(**Alfa) class submarines. Thanks to their reactors and titanium hull, these submarines were faster and more maneuverable than any other class before or since and could outrun the torpedoes available at the time of its prototype deployment. Despite rapid power up/down capabilities and significant efficiency improvements over conventional reactors, catastrophes and the extreme cost of repairs forced their retirement. A similar program in the US using a liquid sodium reactor on the USS *Seawolf* was abandoned within a year of its deployment [7]. By comparison, GenIV lead-cooled reactors must not only be safe but remain in operation for decades. This is due to both construction cost and the amount of radioactive waste produced. The bismuth in the coolant and Cr in the steel become radioactive and have long half lives. Current nuclear waste volumes are quite small in comparison to the possibility of replacing entire reactors on a regular basis. If GenIV reactors are to become a reality there must be significant improvement to the currently available steels. It has been shown that nanostructured materials exhibit significant improvement in radiation damage tolerance [8, 9]. This work will investigate the possibility of improvement through grain size reduction by Equal Channel Angular Extrusion.

Processing

The process of equal channel angular extrusion (ECAE) originated in the USSR with V. Segal and was brought to Texas A&M and the rest of the United States in 1992 [10, 11]. It was further developed here and advancements in tooling materials and design have allowed researchers to process many difficult materials such as shape memory alloys and intermetallics [12, 13]. Despite all the engineering that goes into the tooling, the fundamental process is beautifully simple. A material, typically a bar of round or square cross-section, is extruded through a sharp angle, undergoing large shear as it does so. Since both the inlet and exit channels to this angle are equal in cross section, the material approximately maintains its original dimensions and can be repeatedly extruded. Although the material should shear in a plane between the corners of the elbow, in reality the outside corner becomes "rounded" by material resisting the flow of the extrusion, resulting in a shear zone. Many attempts have been made at modeling the ECAE process, with recent attempts producing more promising results [14, 15, 16]. From the large volume of experimental data, several key elements to designing an extrusion have been identified. These include temperature, extrusion speed, die angle, hydrostatic pressure and wall friction. The extrusions presented in this work used the same 90 degree tool and a fixed speed thought to be the best compromise between cooling and strain-rate effects. Billet temperature, can material and lubricant were varied.

Overview of Thesis

T91 and similar ferritic-martensitic steels have properties near those desired by GenIV reactor designers. Other materials more closely meet designer specifications but are far too costly for power generation structural materials (and will only go up in price) [17]. Given research on other metals for improving radiation damage tolerance and other properties, grain refinement of T91 could enhance its properties enough to allow new, more efficient reactor designs to be commercialized. The next chapter explores the background of T91 applications and properties, giving the scope of the problem faced by materials scientists attempting to enhance its suitability for GenIV and similar applications. It also addresses why ECAE was chosen to attempt grain refinement as a solution to these problems. Chapter III details the experimental methods used to process and characterize the material, as well as specifying the starting materials. Chapter IV contains the significant results of this study with a discussion of the trends, inconsistencies and implications of the data following in Chapters V and VI. Finally, Chapter VII suggests future work in light of the results presented in this thesis.

CHAPTER II
LITERATURE REVIEW

T91

Producers, Composition and Microstructure

Grade 91 steel is produced commercially by several steelmakers worldwide, including Vallourec & Manessman in Germany, Sumitomo in Japan and Wyman Gordon in Texas with Chinese producers starting up as well. Heats from Europe, the US and Japan have been found to vary significantly in strength and performance [18]. This is due to the high sensitivity of T91 to small changes in composition and heat treatment. While the producers listed above are generally considered "safe" there are concerns about Chinese-manufactured steel being marketed under these brands as well as non-existent supposedly US and Japanese brands [19]. All Grade 91 is similar but commercial producers typically sell T91 and P91 as slightly different products for tubing and pressure vessels because of the different heat treatments and service temperatures they are likely to experience.

The composition of T91 was determined using a chromium-nickel balance to tailor the resulting microstructure [20]. Table 1 lists the acceptable ranges for elemental content of the steel. This table refers to Grade 91, encompassing T91 and the almost identical P91.

Table 1. Composition of Grade 91 steel [20].

Element	Weight %
C	0.08-0.12
Mn	0.30-0.60
P	0.01 max
S	0.01 max
Si	0.20-0.50
Cr	8.00-9.50
Mo	0.85-1.05
Ni	0.40 max
V	0.18-0.25
Nb	0.06-0.10
N	0.03-0.07
Al	0.04 max

The key additions to simple 9Cr-1Mo steel are V, Nb and N which help to form precipitates in the steel. As in 9Cr-1Mo, relatively large M23C6 carbides, where M is Cr or Fe, will form during cooling T91. The modifications result in additional precipitates in the form of smaller (1-5nm) M2X and M6X particles where M is V or Nb and X is C or N [21, 22, 23]. The cooling rate from the austenite phase will determine the initial ferrite-martensite ratio in the material as well as the extent and type of precipitates. Cold work prior to tempering may also affect the ferrite-martensite ratio [24]. Tempering, which transforms some of the martensite to ferrite, affects the distribution of carbides, with small carbides disappearing in the tempering range while the large carbides grow. The numerous relatively small precipitates are desired in order to effectively pin the grain boundaries at high temperature [25]. A sketch of the desired microstructure is given in Figure 1. In the sketch a representative single prior austenite grain boundary encloses ferrite and martensite, where some areas are entirely ferrite. Large M23C6 precipitates form primarily on prior austenite boundaries and subgrain boundaries. Small precipitates

form on the lath boundaries and throughout the material. This is the structure that will result in both high strength and ductility.

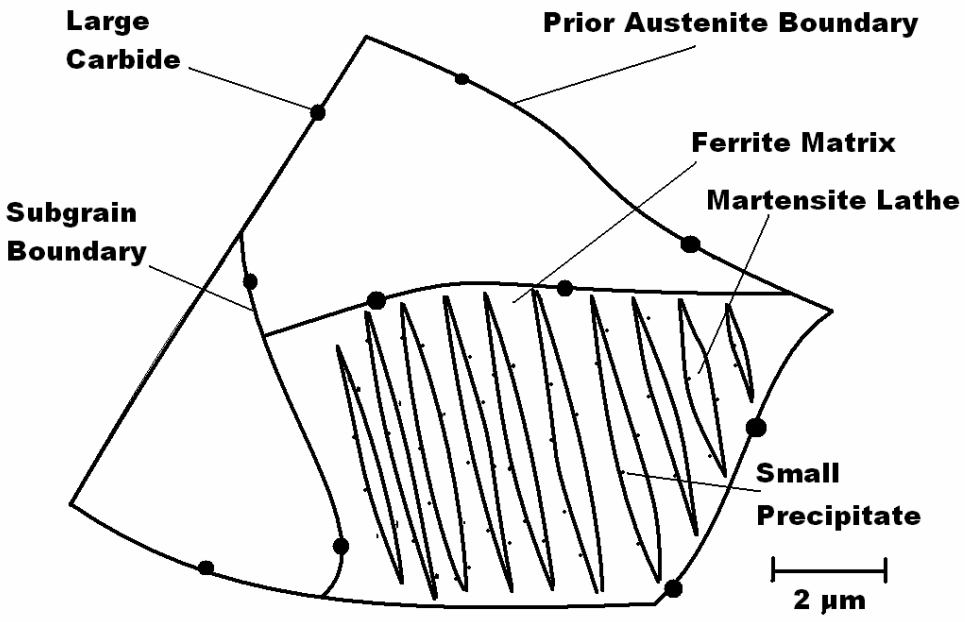

Figure 1. Sketch of tempered T91 microstructure.

Heat Treatment

Proper heat treatment of T91 begins with normalizing at 1050 C so that the material fully austenizes and precipitates dissolve. To achieve a significant concentration of martensite and avoid large carbides, cooling must be faster than 5 C/sec until the martensite start temperature at approximately 400 C and then more slowly until the martensite finish temperature at 200 C [26]. Normally this can be accomplished with thin sections in air. Alpha-ferrite makes up the remaining matrix, with prior austenite boundaries visible. Tempering at 760-790 C for 45-60 minutes follows [27, 21]. Overtempering can cause softening and the aggregation of precipitates, which leads to a

high creep rate. This has occurred in several sections of pipe installed in US power plant superheaters such as that pictured in Figure 2. Undertempering can also cause poor creep performance due to incomplete precipitation. Failure to follow these guidelines has resulted in a number of failures [28, 29, 30]. Additionally, tubing produced to inferior specification in China and marketed as US or Japanese steel has been a problem. In late 2006 the failure of the main steam line in a coal-fired Chinese power plant operating for less than one month killed two persons and injured others. It is thought that both chemistry and poor heat treatment are to blame [19].

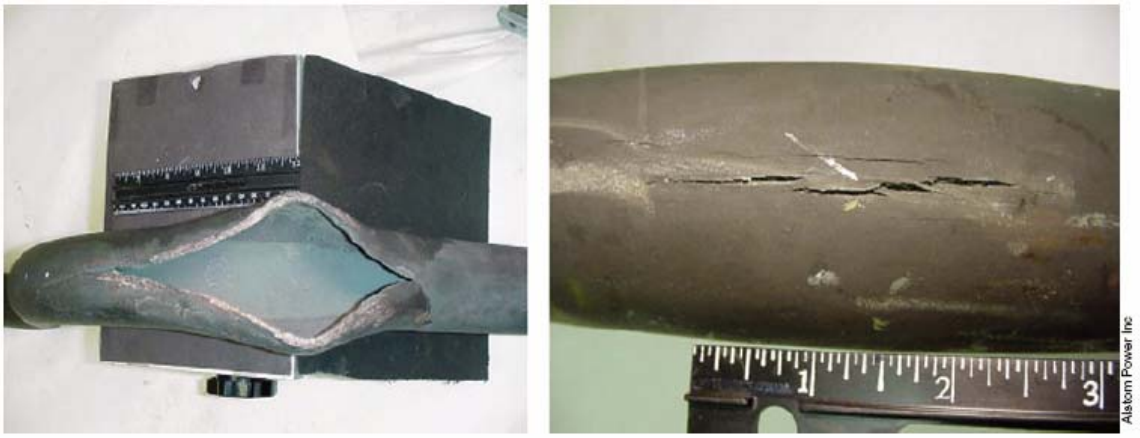

Figure 2. Failure of T91 resuperheater tube after four months of service [31].

Applications

Currently, the most common use of T91 is in fossil fuel power plants. Since the early 1980s engineers have specified grade 91 for high pressure, high temperature sections of power plants with supercritical water working fluid. This steel's high strength compared to other approved alternatives permits thinner walls which result in lower thermal stress.

9Cr-1Mo steel has been studied for use in nuclear power reactors with a liquid metal working fluid since at least 1968 in the United States. [31]. Modified 9Cr-1Mo was developed at Oak Ridge National Laboratory in the 1970s as the benefits of Vanadium addition became clear [32]. The American Society of Mechanical Engineers added the steel to the Boiler and Pressure Vessel code in 1983-4 with piping approval following a decade later [20]. Modified 9Cr-1Mo was further developed by Idaho National Laboratory specifically for liquid metal fast breeder reactor applications and has been widely studied for this and other reactor applications since 1980 [2, 33, 34]. T91 has also been studied as a long-term nuclear waste storage material since 1985 [35]. However, it is unlikely to perform well in this last application. Although its corrosion resistance makes it attractive for possible disposal sites such as salt mines and ocean trenches, the material itself becomes too radioactive, because of the Mo content, to bury near-surface according to DOE rules [36]. This factor is also a consideration when specifying the required lifetime for a GenIV reactor, as the entire system will be radioactive waste at the end of its life.

High Temperature Properties

Grade 91 steel has a well defined service temperature range. Practically, 600 C is the upper limit for long-term operation [37]. However, the radiation damage tolerance of this material shows a dramatic decrease at temperatures below 400 C resulting in swelling and embrittlement [38]. In fact, since the Ductile to Brittle Transition Temperature (DBTT) of this material is near 0C, even room temperature operation is not advised [39]. Operating temperatures below 566 C may result in stress corrosion cracking if heat treatment was imperfect [29]. However, grain growth at these

temperatures is limited only by precipitates, requiring accurate heat treatment and composition to control their distribution if creep is to be prevented. Upper service limit creep properties typical of Grade 91 are presented in Figure 3.

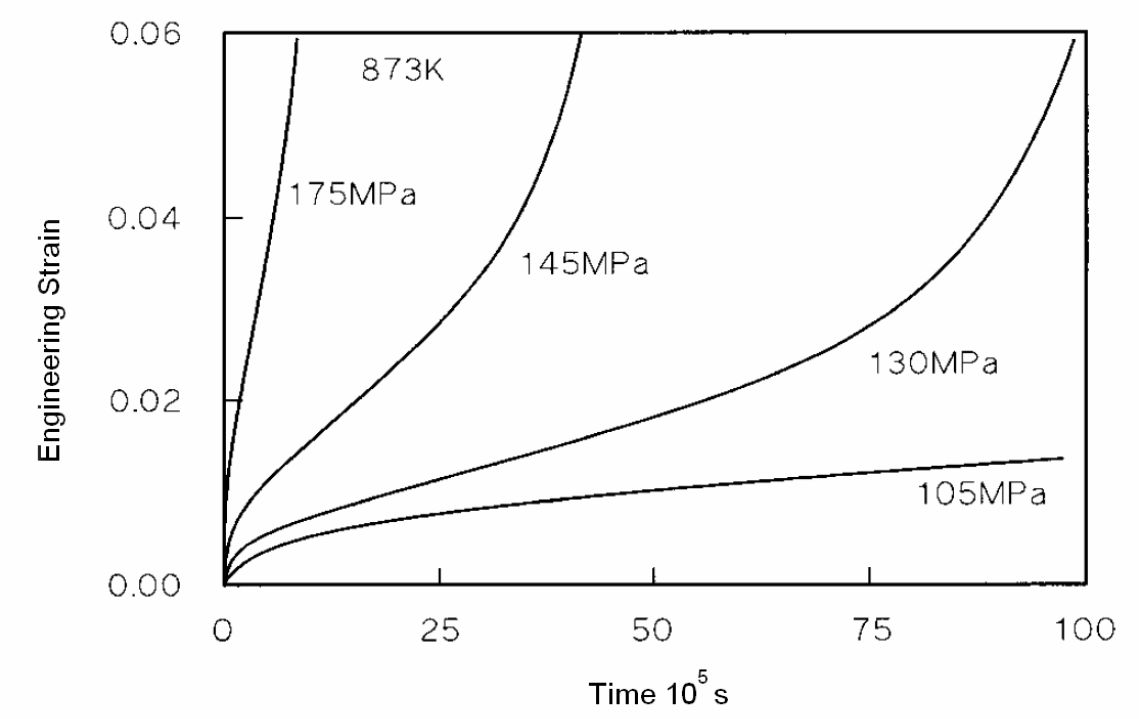

Figure 3. Creep of Grade 91 at 600 C [21].

It is apparent that at this temperature the steel cannot sustain stress levels above 100 Mpa. However, T91 shows good thermal stress performance and thick walled tubing can be used for many applications. Fortunately, the liquid metal GenIV reactors will operate at relatively low pressures, so this stress limit does not pose a problem with their use in this application [40]. There is some interest in using T91 in the lower temperature sections of new power stations that will require Hastelloy or similar expensive alloys for their high-temperature sections. This poses additional welding challenge but also

necessitates the investigation of how extreme the service conditions of modified 9Cr-1Mo can be. Figure 4 shows creep rupture testing results of T91 at varying temperatures. These high temperature failures are attributed to the dissolution of MX carbides and the coarsening of M23C6.

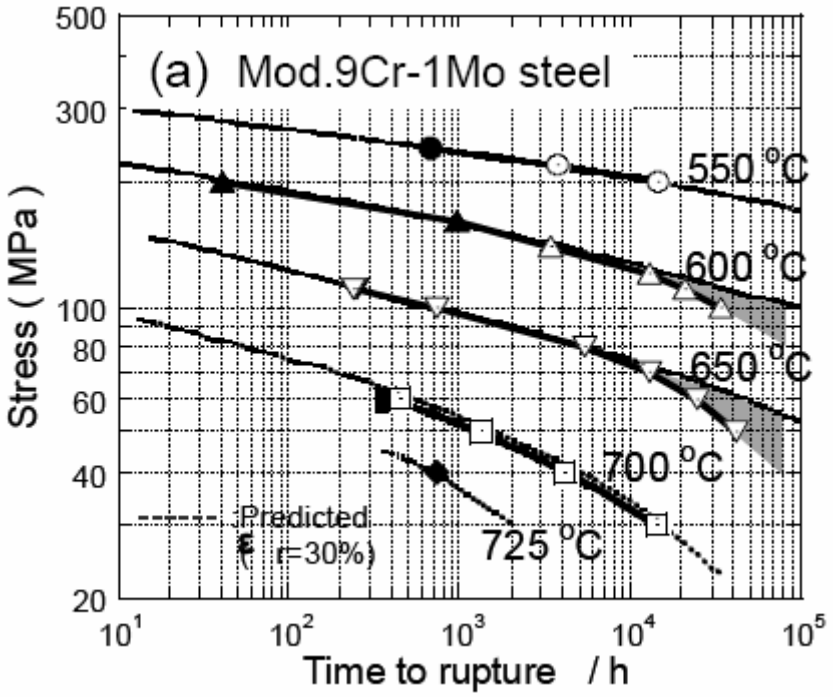

Figure 4. Creep rupture testing of T91 [22].

Aging at GenIV reactor temperatures has the effect of forming additional precipitates and generating new and larger voids in the material [41, 42]. Additionally, phase transformation from martensite to the more stable ferrite can occur over time [42]. Even with stable or decreasing grain size, hardness drops over time due to the dissolution of precipitates. The long-term use of this material in industry at high temperatures and pressures has allowed some insight into how T91 might behave in long-term GenIV

applications. One early example is the study conducted by Swindeman on a superheater tube in 1995. The material saw 15 years of service in a thermally and corrosively challenging environment. This revealed grain growth as a concern above 400 C as coarsening occurred until M23C6 carbides or aging-induced precipitates pinned the boundaries. Oxidation was minimal for most of the material. Unfortunately for the engineers, the aged microstructure seems to vary significantly under slightly different temperature and stress levels when comparing the in-service material to other published long-term aging and creep studies. Welds, particularly with dissimilar stainless steels, were also a concern, as they were the primary area of oxidation and cracking [43]. Since proper welding is crucial to the durability of installed components it will be discussed further.

Welding

Over the years, power contractors have developed their own welding methods for T91 steel as the ASTM-specified minimums may not result in the desired microstructure [26]. However, the Electric Power Research Institute summarizes the essentials:

> "Welding P91 requires a complex five-step process. After fitting the pipe, welders then preheat the weld area to the pre-weld temperature (400 degrees F or 204 degrees C). Next, the area is welded carefully, after which the weld must cool to at least 200 degrees F (93 degrees C), but preferably to room temperature. To complete the weld, the area must be heated to a post weld heat temperature (PWHT) of 1375-1400 degrees F (746-760 degrees C)." [44]

They also point out that this PWHT temperature can adversely affect the strength of carbon steel or plain 9Cr-1Mo that might be joined to the T91. Dissimilar steels, especially other ferritic-martensitic steels, can be welded with T91 using standard procedures and T91 filler. However, PWHT becomes even more crucial in these cases, as deviations can cause rapid failure. Brozda and Zeman provide a comprehensive study of temperature deviation in PWHT, showing that a case of weld cracking during assembly of resuperheater tubing was caused by tempering that varied from 600 C to 700 C in different sections [28]. The literature contains numerous examples of in-service failure at welds due to improper PWHT [29, 43].

Corrosion

T91 has a relatively low Cr content compared to most ferritic stainless steels and thus has a lowered corrosion resistance. However, under the right conditions it can sustain high temperature service in a corrosive environment. Many corrosion studies on T91 are carried out in water since the steel's current commercial applications are primarily in steam power generation. One such study used supercritical water at 370 C and 500C, demonstrating that ananodic dissolution was the main erosion mechanism at 370 C while oxidation dominated at 500C. In both cases a layer of magnetite formed over oxide. Most importantly, the study found a 40% increased crack growth rate because the brittle surface oxide easily cracked to allow water into expanding cracks [45]. This highlights the need to maintain operating conditions that do not encourage crack growth and allow stable oxides to quickly grow and repair damage.

In boiler applications, fireside corrosion of T91 is minimal in most long-term studies. However, in one case a .38mm/year loss was found, probably due to locally

higher temperatures [46]. Steam-side studies matched well with laboratory-based data, confirming a 600 C upper temperature limit and good performance at 560 C and lower. One specimen saw 560-580 C service for 16 years and had a stable .2mm oxide layer [46]. Oxidation of T91 seems similar to 9Cr-1Mo, which has examples of stable oxides at up to 600 C for 20 years [47].

For piping between a boiler and turbine, one must consider the complementary effect of erosion-corrosion due to the high velocity of steam. Particles from the turbine can travel within the line and impact oxide layers at high speed, shattering them and allowing the material underneath to corrode [48]. Additionally, the steam's pH can be lowered by organics that leak into the system. Given these factors, the most important considerations in steam line applications are to generate a tough oxide layer and to keep particles out of the loop. However, GenIV nuclear reactors will contain entirely different environments and therefore different considerations.

While sodium cooling produces a higher efficiency than liquid lead bismuth, safety concerns favor the latter [49]. The corrosive effect of liquid lead-bismuth on T91 has been well studied under laboratory conditions. Austenitic stainless steels like 316L perform quite poorly in this application. This is due to their high nickel content, which is leeched out by the coolant, allowing deep penetration of the Pb-Bi [50]. However, even well-performing steels like T91 require proper operating conditions to survive in flowing Pb-Bi. One key aspect of this is the control of oxygen in the lines. If there is not enough to quickly re-form any damaged oxide layer, the Pb-Bi will penetrate into the steel and dissolve it. As in steam lines, erosion-corrosion is a problem with Pb-Bi systems. However, the mechanism does not require particles, instead relying on Pb-Bi penetration

to break up oxides which are then carried away from the surface [50]. This effect is illustrated in Figure 5.

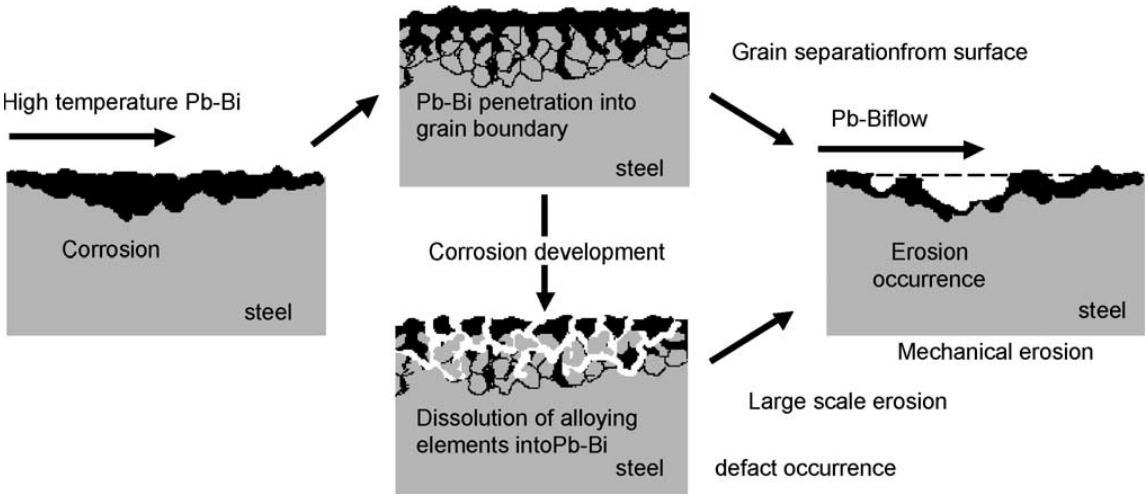

Figure 5. Corrosion-erosion mechanism under liquid metal flow [50].

An oxide layer more robust than the Cr oxides in T91 has been sought for some time, with a great deal of focus on coatings. However, one recently developed alloy forms a layer of alumina on the surface and may be a practical alternative to coatings [51]. However, this alloy would rapidly corrode if a crack formed in the protective alumina since it is 20% Ni and is therefore unlikely to be used in a liquid metal reactor. Details like this illustrate the need for a thorough investigation before a material is suited for advanced applications like GenIV reactors. In another example, it is suspected that simultaneous exposure to radiation and liquid metal corrosion may increase the damage rate to T91 and similar steels beyond the sum of the two effects alone. This will be discussed further in the next section. It should be noted that this is a concern for supercritical water applications as well. In one study, 20 Displacements per atom (Dpa)

proton implantation prior to fluid exposure promoted intergranular cracking in HT9, a 12% Cr ferritic-martensitic steel, but did not show this effect in T91 [52]. Bear in mind that this may not be representative of long-term neutron damage exposure.

Radiation Damage Tolerance

The major effects of radiation damage are swelling, embrittlement and eventually loss of material. A radiation damage tolerant material must be able to absorb particle radiation while delaying the onset of these effects. BCC stainless steels like T91 have superior radiation tolerance compared to typical austenitic steels. This is due in part to the effect of Cr segregation to the surface of He bubbles within the microstructure, inhibiting their expansion and migration more effectively than Ni in austenitic steels [53, 54]. Toloczko *et al* compare the performance of HT9 and 9Cr-1Mo steel under high temperature irradiation up to 200 Dpa at 400 C while undergoing stress up to 200MPa. The HT9 and unmodified 9Cr-1Mo performed similarly under no load, with less than 1% strain. However, when analyzing the loaded specimens it was shown that the 9Cr-1Mo had a linear creep rate while HT9's was exponential. On the other hand, 9Cr-1Mo showed stress-insensitive swelling damage of almost 3% at 200 Dpa, a level not reached by HT9 until the highest stress in the study [55]. In another study at 203 Dpa and temperatures from 400 C to 425 C, mean swelling of T91 was 1.75% while HT9 showed almost no swelling in most samples [56]. By comparison, 316 stainless steel reaches a 20% saturation swelling at this dose with Ni ions at 627 C and 250% with protons at 625 C [54, 57]. Note that the Toloczko and Gelles studies were conducted under essentially the same conditions but produced difference results for HT9, their common material. This highlights the difficulty in conducting these studies. It is challenging to maintain a

uniform, long term ion or neutron beam over several samples and the material is sensitive to chemistry and heat treatment. Additionally, these studies are expensive, discouraging much repetition of the work.

While swelling changes the fluid flow behavior of a line, embrittlement is more of a threat to the life of the plant (and its workers). In addition to damage clusters, embrittlement can be caused by Radiation Induced Segregation (RIS). Mathon reports RIS causing phase change in alpha ferrite such that Cr-rich alpha'-ferrite appears at close to grain boundaries at temperatures up to 600C. Huang and Hamilton showed that embrittlement of T91 and HT9 saturates at 30 Dpa until at least 100 Dpa for neutron irradiation at 55 C [58]. Fracture toughness testing at room to high temperatures showed that HT9 demonstrated better performance than T91 after this low temperature irradiation. Room temperature toughness of T91 dropped by 25-50% while some HT9 actually increased in toughness. Increasing dose results in an increase in the DBTT. One short-term study showed an increase of T91's DBTT from -54 C to 165 C with only a 0.2 Dpa dose of He ions [59]. Unfortunately, no studies on cold-worked T91 are currently available in the literature but rolling 316 has been shown to enhance post-irradiation fracture toughness compared to annealed material [60]. Another study showed no such effect [61] while an additional study showed that saturation strength was the same but that the cold-worked 316 had a delayed swelling onset [54]. This same study points to reversing trends (softening to embrittlement) in several materials depending on the implantation regime. It should be noted that even at low dose, the T91 in this study showed less embrittlement than the 316L. All of this highlights the difficulty in predicting the effective lifetime of these materials in actual application environments.

It has been suspected that the effects of radiation damage would enhance corrosive effects in liquid lead cooled reactors. So far it has not been shown that liquid metal embrittlement is enhanced by irradiation in both T91 and 316L [62, 63]. However, these experiments used a low dose and the irradiation was not carried out simultaneous with corrosion in one study. Additionally, while liquid metal embrittlement is one corrosion factor, it is necessary to discern the long-term effects of simultaneous irradiation and material loss by corrosion-erosion in flowing lead-bismuth. It is hoped that an experiment being set up by collaborators at Los Alamos National Laboratory (LANL) will provide data on this subject within the next few years.

In a review of available data, Loomis shows that ion implantation is a good neutron damage simulation in most cases, including ferritic steels. However, 316 stainless steel and, in the limited available data, copper were shown to begin a steady state damage accumulation at a lower dose of neutrons than ions, as well as having a significantly higher steady state damage rate [64]. This should be kept in mind when comparing ion implantation damage of FCC and BCC steels.

Like many steels, there are competing damage accumulation and diffusion mechanisms that result in a temperature range in which this material shows the most damage tolerance. One basic explanation of this phenomenon has been presented by Todd Allen in his radiation damage class at the University of Wisconsin in Figure 6. A more detailed explanation with a modeling framework can be found in the literature [65].

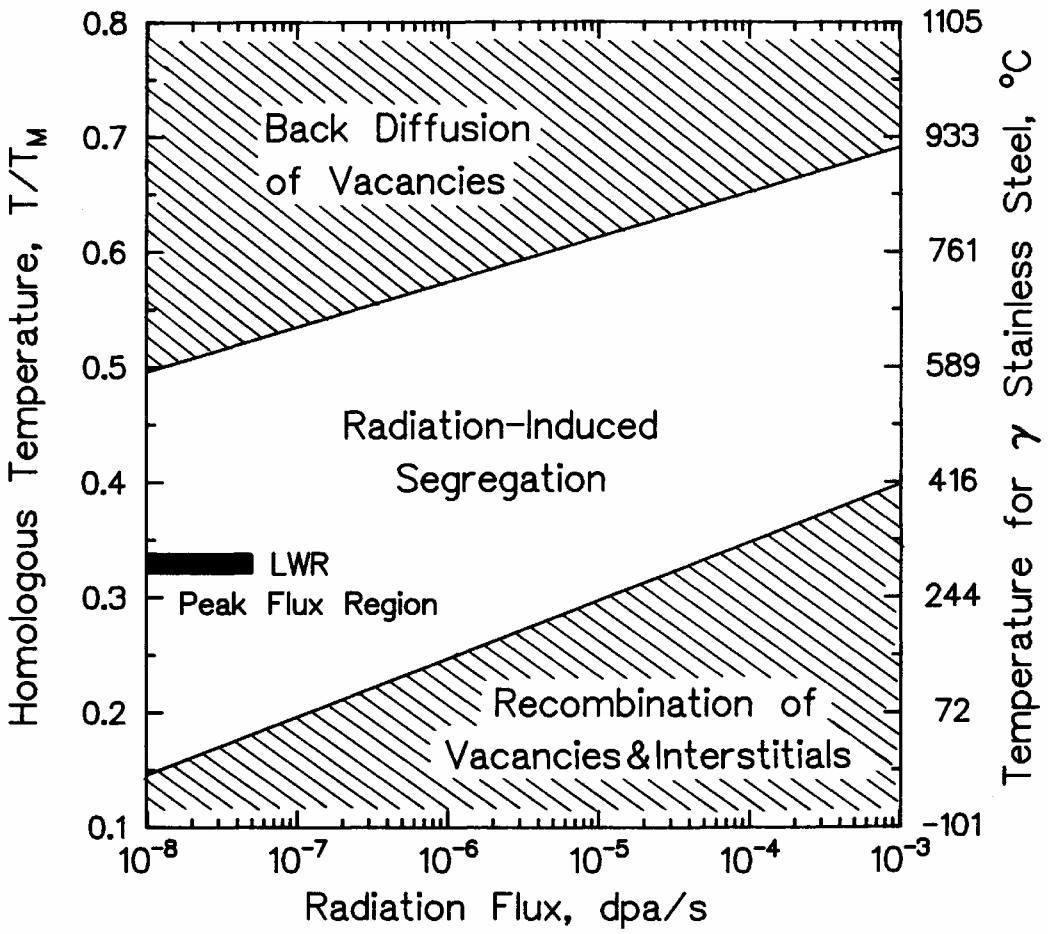

Figure 6. Radiation damage factors in austenitic stainless steel [66].

The challenge from a materials design standpoint is to match the material's radiation tolerance ranges with the operating temperature while avoiding creep. Since many of the diffusion mechanisms responsible for damage recovery are also responsible for creep, this is non-trivial. An overview of the temperature/flux/strain relationships and the resulting desired operating conditions for various materials is shown in the proceedings of the High Temperature Reactor Materials Workshop 2002 [17].

ECAE

Equal Channel Angular Extrusion (ECAE) was developed by Segal as a method of inducing a theoretically unlimited amount of simple shear in materials [67, 10]. Unfortunately, the West had limited access to his original work since it was carried out behind the Iron Curtain. However, after the fall of the Soviet Union and Segal's immigration to the United States, the process was brought to Texas A&M University. Today there is an extensive body of work on ECAE generated by laboratories across the globe, some of which will be highlighted in this discussion.

The basic die design and process of ECAE can be seen in Figure 7. Two channels with equal cross-sectional areas intersect at a specified angle φ. This angle can be varied from 90 to 180 but is most often perpendicular as this imparts the highest shear strain per extrusion. This shear ideally takes place at the plane between the corners of the die. However, since the die will not be perfectly sharp and the material being extruded tends flow along a rounded outside corner, shear will actually occur over the fan-shaped zone defined by angle ω. The shear strain imparted in the extruded material is given by [68]

$$\gamma = (2/\sqrt{3}) N\cot \varphi \qquad (1)$$

This gives a calculated strain of 1.16 for a single pass through a right angle die. Despite the fact that the derivation of this equation does not factor in ω, which Segal later changed, it is a close approximation in most materials and processing conditions [69, 70]. The strain is quite uniform with the exception of the ends and walls of the extruded billet. The procedure does not require the area reduction that limits strain in conventional cold work techniques. Therefore, strain can be increased by repeatedly passing the material

through the die. The "route" or billet orientation for each pass has a dramatic influence on the resulting texture and other microstructural properties. Reference will be made to the plane from which samples are taken. These planes are defined by Figure 7 and are in reference to the last pass undergone by the material.

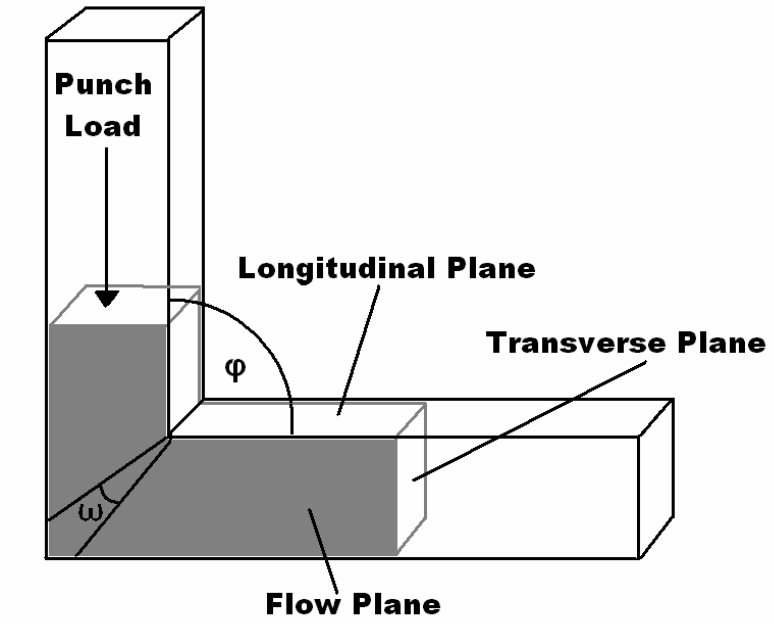

Figure 7. Illustration of the ECAE process.

Rotating the billet around its long axis between extrusions as dictated by a predetermined route can generate a particular desired texture. These routes are discussed by Iwahashi et al [71]. For this work route B was used, in which the billet is rotated 90 degrees between passes. The routes determine the amount and shape of the fully worked region within the billet. Examples of these regions are shown in Segal's work [11]. Perhaps the simplest way to conceptualize ECAE is to simply see its affect on grains. An

example of a single pass of ECAE on annealed, large grained pure copper can be seen in Figure 8.

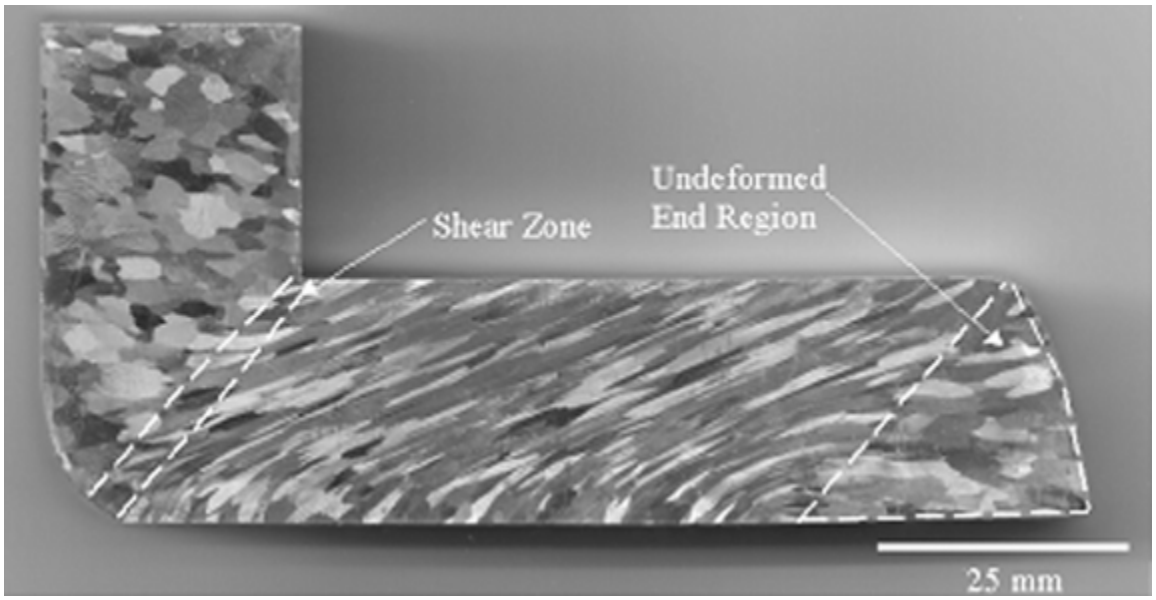

Figure 8. Incomplete single pass ECAE on cast copper. The surface has been polished and etched.

ECAE has been found to be suitable for refining grain size, increasing strength or ductility and numerous other applications in a wide range of materials. Processed materials include FCC copper [68], nickel [72], aluminum [73] and austenitic stainless steels [74], BCC iron [75] and tantalum [76], HCP magnesium [77] and titanium [78] as well as some more complex materials like bismuth antimony [13] and shape memory alloys [74]. ECAE can consolidate powders, which is especially useful for creating bulk metallic glass materials [79]. Additionally, composites have been fabricated with metallic glass/metal [80], metal/ceramic [81] and polymer/fiber [82]. Cast metal can be processed such that it takes on metal/metal composite characteristics, such as drawing out

filaments of one material within the surrounding second phase [68]. Not only can ECAE process this range of materials, it has been shown to be able to scale up without changing its processing capabilities [83]. All this can be done with simple tooling such as a conventional hydraulic press and two-piece die. However, additional more complex systems are required to overcome some of the problems with ECAE. These problems include material loss, plastic strain limits in the material, load requirements, material shape requirements and the need to machine or otherwise reshape the billet between passes. Advanced tooling coupled with heat treatment and special processing routes can overcome some of these problems for many engineering materials. It is thanks to some of these refinements that ECAE was chosen to process T91 for this study.

Deficiencies and Rationale for Study

There is a significant interest in ferritic-martensitic steels throughout the nuclear materials community. Since this class is so promising, many projects are being funded in the hopes of developing a more complete picture of the various alloys within the group. Any trends that can be identified may help develop materials fully capable of GenIV service. Problems related to all the sections covered in this review are being attacked from several angles. Most of these approaches relate to chemistry, particle addition, heat treatment and coatings. This work will focus on plastic deformation processing of a material that is already well understood in these other areas. It has been shown that conventional low-strain cold work improved the radiation tolerance of stainless steel and that nanoscale microstructure produced a dramatic improvement in other materials [60]. However, there was a gap in the literature between this mildly refined microstructure and true nanoscale features. Also, there is little work on ECAE of ferritic-martensitic steels

[84]. Given this, it is prudent to investigate the capability of SPD to improve T91 as a possible GenIV bulk material candidate. T91 is an appropriate study material because of its extensive coverage in the literature and promising starting properties. ECAE was chosen for SPD because of its capability to impart large strains on large material sizes as well as its extensive coverage in the literature.

Fortunately this work has attracted some interest prior to publication. Collaborators are investigating corrosion and radiation damage affects that cannot be practically studied at Texas A&M University. Hopefully this broad investigation of worked T91 will aid project managers in the decades-old quest for a cost-effective structural material capable of 30-40 year service life in a liquid metal cooled nuclear reactor.

CHAPTER III
EXPERIMENTAL PROCEDURES

Materials

Two T91 materials were used in this work. They were received from collaborators at Los Alamos National Lab and are referred to as LA1 and LA2. Their chemical compositions, LA1 as nominal and LA2 from chemical analysis, are shown in Table 2. Note that LA2 contains a relatively high amount of Vanadium, low Phosphorus and is generally more heavily alloyed than the LA1.

Table 2. T91 chemical composition of starting materials.

Material	**LA1**	**LA2**
Method	nominal	DC plasma
Fe	87.5-90	88
Cr	8-9.5	9.23-9.26
Mo	0.85-1.05	0.97
Mn	0.3-0.6	0.52
Ni	0.4	0.45
C	0.07-0.14	0.077-0.082
Si	0.2-0.5	0.31-0.34
V	0.18-0.25	0.28
P	0.02	0.006
S	0.01	0.002
W		0.016-0.021
O		0.012
N		0.008
Co		0.007
Cu		0.022
Ti		0.003
Al		0.006

Processing

ECAE processing was carried out in a sliding wall die designed by Robert Barber and Dr. K. T. Hartwig. This was facilitated by an MTS-controlled 225 ton (250 short ton) hydraulic press. The extrusion rate was 1.27 cm/s (0.5 in/s) in all cases. Temperature control was accomplished by maintaining the die at 300 C and placing any billets requiring a higher processing temperature in an adjacent oven for one hour prior to extrusion. The large temperature differential in some extrusions required that the researchers work quickly so that cooling of the billet was not significant. Typically the processing time was 20-25 seconds from removal from the furnace to quenching.

Starting material and processing method are linked to a corresponding billet identifier in Table 3. 1AR and 2AR are the as-received materials from the first (LA1) and second (LA2) batches. Additionally, 1ARHT will be used to denote 1AR/LA1 material that has been heat treated at 1050 C for one hour in a vacuum furnace and vacuum cooled. 1ARHT was the starting material for #20 and #21.

Table 3. Billet identifier with corresponding processing data.

Identifier	Chemistry	Route	Extrusion Temp
1AR	LA1		As Received
#1	LA1	2B	300 C
#3	LA1	1	700 C
#4	LA1	2B	700, 600 C
#20	LA1	1	700 C
#21	LA1	2B	600 C
2AR	LA2		As Received
#6	LA2	3B	700 C
#10	LA2	1	500 C
#18	LA2	1	600 C

Material for ECAE processing was prepared utilizing wire Electrical Discharge Machining (EDM) and conventional machining. EDM was used to cut material from the received pieces so that little material was wasted. Samples #1-4 were cut as two 6mm (0.25 inch) diameter rods from the received piece using a Mitsubishi FX10 wire EDM. These rods were sawn to approximately 2.5 cm (1 inch) long pieces. To carry these small samples around the channel, billets were made from Ni200 alloy plate. These billets were cut and machined using a band saw and mill to approximately 2.49 x 2.46 x 10 cm (0.980 x 0.970 x 4 inch) to fit the 2.5 cm (1 inch) square cross section tool. The billets must be machined to under 2.5 cm (1 inch) square in order to account for thermal expansion and a coating of lubricant. The billets were then drilled with 7.1 mm (9/32 inch) holes to place the samples midway down the length of the billet. These samples

were wrapped with 0.25 mm (0.010 inch) brass shim material before being placed in the billet to facilitate identification of the sample during extraction. The holes were then plugged with 6.4 mm (0.25 inch) diameter stainless stock material to prevent the samples from moving outward in the hole during extrusion. Rods of four additional materials were included in the nickel cans with #1-4. Vacuum sealing the samples was deemed unnecessary at the temperatures of these extrusions. A schematic of the canned LA1 samples is shown in Figure 9.

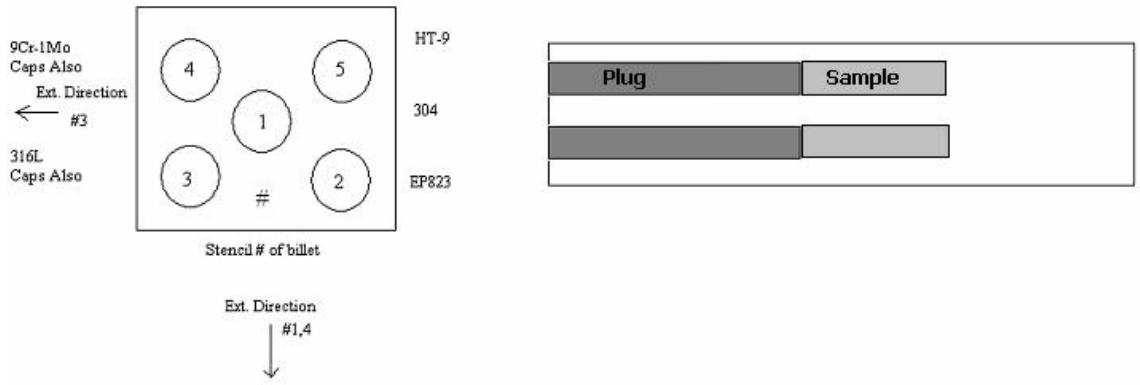

Figure 9. Schematic of LA1 samples before processing.

The LA2 samples arrived as a 2.5 x 10.8 x 10.8 cm (1 x 4.25 x 4.25 inch) block. By this time the group had acquired a Mitsubishi FX10 wire EDM, which was used to section the block into four billets. Billets for the second set of extrusions using the LA1 material (#20, #21) were created similarly to the first, with a few exceptions. The samples were EDM cut to 5 x 1.3 x 106 mm (0.2 x 0.5 x 4 inch) and corresponding rectangular holes were EDM cut in the 15.2 cm (6 in) long billets. This larger size would allow for tensile and other large samples to be obtained from LA1 material. Ni-200 plugs were

inserted into the billets and tack welded in place after the brass wrapped samples were inserted.

Prior to processing the billets were painted with lubricant, the choice of which was temperature dependant. Low temperature billets were painted with Loctite Silver Grade Antisieze, a graphite and oil based lubricant. High temperature billets were initially painted with this as well. However, due to issues to be discussed later, a change was made to Acheson Deltaglaze 153, a water-based solution of lead-free glass and acrylic microbeads. After drying, 300 C billets were placed in the entry channel of the tool and left for one hour, while 600 C and 700 C billets were placed in a nearby furnace at temperature for the same time. In high temperature extrusions the operator would remove the billet from the furnace with tongs, drop it into the entry channel, close the ram over the channel, and press start. Low temperature extrusions simply required starting. Samples were quickly removed from the tool and quenched. The time from removal to quenching was typically 5 seconds or less. The extrusions took 14 seconds and high temperature extrusions required approximately 5 seconds to move from the oven to the tool. Press load and die temperature were recorded during the extrusions. Dimensions of the extruded billet were recorded after it cooled. The process was repeated for each extrusion, machining the billet down to size between passes.

The sample extraction process varied depending on the sample geometry. LA1 nickel-canned rods were removed by milling away the billet until the brass sheet wrapping the sample was exposed, at which point a hammer and chisel were used to pry away the can material and pop out the sample. LA1 R2 samples were exposed via EDM to conserve the nickel cans, which have significant scrap value. The large LA2 samples

needed nothing beyond machining and grinding away the glass lubricant before they were ready for sectioning. This removal of lubricant or oxides is necessary before any EDM cutting because the process cannot cut through insulating material. Samples were taken away from edges and the end zones that would not have undergone uniform deformation. After exposure/removal, samples were prepared for further testing using methods to be described in the section corresponding to their examination. Rods from the LA1 extrusions were cut in half to send to collaborators at Los Alamos National Lab. Rectangular samples were taken from LA2 material for corrosion testing at Los Alamos and at the University of Wisconsin. The Los Alamos samples were coated via laser deposition with strips of TiN in order to prevent corrosion under a reference area.

Microhardness

Microhardness samples were prepared so as to use as little material as possible without compromising data quality. Typically, 6 mm (0.25 inch) diameter discs were cut at approximately 1 mm thickness from sample rods with a Buehler Isomet 1000 diamond wafering saw. The rods were either extracted from an ECAE can intact or wire EDM cut from larger samples. It was found that the most efficient method to produce a quality polished surface was a relatively standard procedure. The disks were de-burred with a file then affixed to Pyrex cylinders using Crystal Bond, a wax that provides a strong bond at room temperature. These 10 mm diameter Pyrex cylinders fit into a Gatan 623 disc grinder that facilitated the process of grinding the upper and lower sample surfaces parallel to each other. Eventually, it was found that 10 mm aluminum Scanning Electron Microscope (SEM) stubs could also be used to mount larger microhardness samples that would not be sensitive to imperfections in the mount surface. Thereafter the more

expensive Pyrex cylinders were reserved for Transmission Electron Microscope (TEM) sample prep. The discs were ground on an Allied High Tech MetPrep rotary polisher using 400, 600, 800, 1000 and 1200 grit silicon carbide paper and a constant water flow followed by polishing with 0.05 μm silica colloidal suspension on Buehler Texmet cloth. This was eventually performed under a laminar flow fume hood that, combined with thorough rinsing with deionized water between steps, nearly eliminated scratch-causing particles in the later steps. The samples and cylinders were placed in an acetone bath for approximately half an hour to dissolve away the crystal bond and free the sample then cleaned with methanol. Even with relatively simple sample preparation such as this, attention to cleanliness of the samples, polisher and polishing papers made a large difference in the resulting surface quality.

Microhardness measurements were performed with a Fischerscope 2000 which is a hybrid between a conventional microhardness tester and a nanoindenter capable of generating stress-strain curves for each indent. The machine has an automated x-y stage and digital camera, allowing for the selection of a series of points in clean areas of the material. The tip in this machine is a Vickers pyramid but software translates the stress-strain data to other useful standard information such as Martens hardness and indentation modulus. Measurement trends were verified using a Buehler Micromet II. Measurements were typically taken in a grid spanning the sample at 2000N load which equated to approximately 5 μm penetration depth in these materials. This is the maximum load setting for the Fischerscope but was chosen because of its correlation to mid-range settings on the Micromet and generally accepted loads in the literature. Additionally, hardness values measured by the Fisherscope are essentially unchanged

from 2.5 µm to 5 µm. Load time was 30 seconds for both machines with 5 second creep time specified for the Fischerscope.

Indentation modulus (EIT), indentation hardness (HIT), Martens harness (HM), and Vickers hardness (HV) were recorded along with the load curves for all specimens. Indents were visually examined using the digital microscope to verify that no cracking occurred and that the indenter did not impinge on a surface imperfection such as an imbedded particle. This ability to see the indents with a microscope as in a conventional hardness indenter coupled with the stress-strain curves was helpful in determining when a data point was in error. Although care was taken to avoid surface imperfections, the Fischerscope would in some instances shift its pattern of indents so that oxides or other imperfections affected the impression. Additionally, in some instances there were no visually obvious problems with the indents. Figure 10 illustrates a set of force vs. displacement curves in which an error has occurred. This error would be accompanied by a modulus reading far from the bulk modulus.

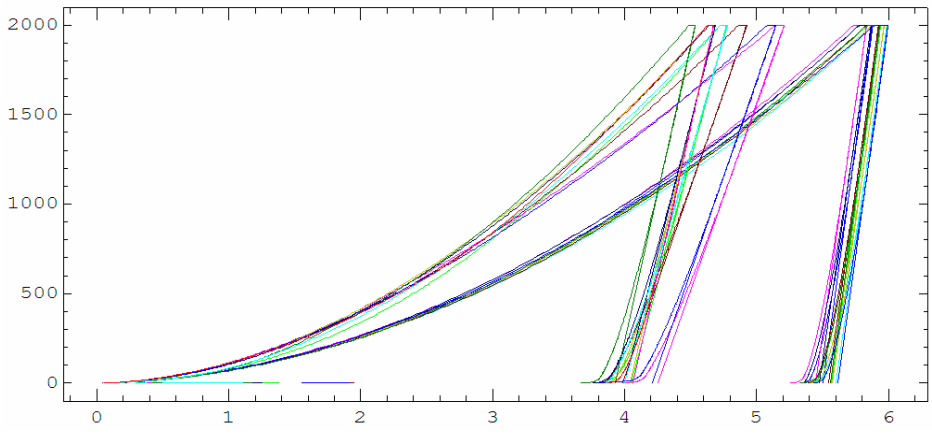

Figure 10. Example load vs. displacement curves in which an unknown error has occurred in several measurements. The leftmost curves have a significantly lower modulus than expected.

Transmission Electron Microscopy

Sample preparation for TEM was performed similarly to that described in the microhardness preparation. LA2 and rectangular LA1 samples were EDM cut so that a 3mm diameter rod could be sectioned into a disc to eventually fit within the TEM sample holder. Samples from #1-4 were prepared by several methods. The most successful involved cutting a strip from a sample disc with the diamond saw. The samples were polished in the same manner as for microhardness, removed from the Pyrex cylinders by dissolving the wax in acetone, flipped and then re-bonded. They were then ground to 70-90 μm thickness and placed in a Gatan 656 dimpler. Using 10 μm diluted diamond paste and a copper wheel the sample was ground to 25 μm thickness then polished with a cloth wheel and 6 μm diluted diamond paste for 5 minutes. Care was taken not to go too far with the dimpler, as a sample with a hole at this stage was unlikely to produce good images. The sample was then removed from the cylinder. The EDM cut discs went directly into the Gatan 691 Precision Ion Polishing System (PIPS). The earlier diamond saw cut irregular samples were attached to molybdenum TEM sample rings with epoxy and milled in the Fischione 1010 ion mill. Milling was done in varying time segments, regularly checking for the development of a hole with a light source below the sample. This was facilitated in the (PIPS) by a microscope that swings over the sample viewing window.

TEM images were collected on a Jeol 2010 using Kodak film. Typically, the sample was inspected at increasing magnification, and then several representative micrographs were taken at a resolution to best capture the thin area. Selected Area Diffraction (SAD) patterns were taken using an aperture large enough to cover most of

the imaged area except when inspecting a particular point of interest such as a carbide particle. The films were developed using standard darkroom techniques and digitized with a negative scanner. Once they had been digitized, Adobe Photoshop was used to adjust contrast and brightness, measure feature sizes and index diffraction patterns. Average feature size measurement was performed by the lineal intercept method. Features include grains and subgrains, as it is difficult to discern one boundary type from another in TEM micrographs. This technique utilizes a series of parallel lines of fixed, known length and equal spacing. Horizontal and vertical lines are used to counteract the effect of morphology on the measurement. The boundary intersections along each line are counted with any intersections at a triple point being weighted by 1.5 and intersections at the very end of a line weighted by 0.5. By division, the average number of grains per length is obtained. This mean lineal intercept length is multiplied by 1.5 to obtain the approximate spherical grain size. Although more exact measurements can be obtained when measurements are taken from three orthogonal planes, approximating the grains as spheres is a common practice. It should be noted that the error due to this approximation becomes more significant as real aspect ratio increases.

X-Ray Diffraction

X-Ray Diffraction (XRD) samples were the same discs used for microhardness measurements. The XRD data was taken after polishing but before microhardness testing or other surface damaging procedures. Care was taken to ensure that the sample surfaces were free of attached particles, water spots, and other possible contaminants that might deteriorate the x-ray baseline. A short-arm Bruker-AXS D8 was used for all XRD data. Measurements were taken using a copper source at 40 keV and 30 mA with a 1 mm slit.

Samples were mounted within a ring using children's craft putty such that the surface of the sample was parallel to that of the ring. Figure 11 is an image of this system. This simple setup for repeatable sample placement ensured that few data collection procedures were stopped due to misalignment. Typically, a 0.1 degree/sec scan rate was used to cover a 10-100 degree 2 Theta range. Peak matching was preformed with the Bruker-supplied database.

Figure 11. Sample mount for XRD

Tensile Testing

Tensile testing was performed with an MTS machine at a cross head speed of 0.04 in/min and a sampling rate of 10 Hz. An MTS 632-53 extensometer spanning nearly the entire gage length was used to collect strain data. One inch dog bone specimens were EDM cut to the specifications of Figure 12.

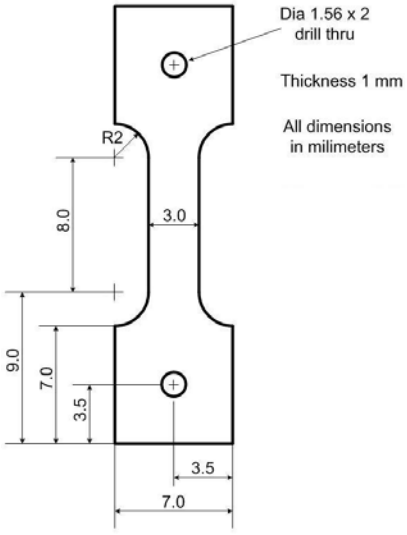

Figure 12. Tensile coupon schematic courtesy of Burak Basaran.

The samples were deburred and sanded to remove the porous oxidized brass layer left by the EDM then measured with calipers before testing. Samples were pulled to failure then bagged and labeled for later examination. Data analysis was performed in Excel using a line fit to the elastic region for modulus and 0.02 offset for yield strength.

SEM images were acquired with a Jeol 6400 using a PGT Avalon digitizer. Secondary electron images were taken at 15 keV and 3x10^-11 A spot size. The post-test tensile specimens were rinsed with ethanol and mounted with several methods. They were first simply stood on end on a flat stub covered in carbon tape. Sample drift, most likely due to heating of the sample, demanded a more secure system, so the samples were clamped using a spring-loaded stub that sandwiched the specimen between two plates pictured in Figure 13. Samples were also affixed by carbon tape along their long side to a stepped stub. Despite the help of the microscopy staff, very slow sample drift remained a problem, limiting Energy Dispersive x-ray Spectroscopy (EDS) imaging to low-

resolution for the tensile samples. EDS was performed using a PGT IMIX attached to the SEM. Several attempts at etching specimens to observe grain size were made without success. However, Peter Hosemann at LANL etched samples from billets 1, 3 and 4 before and after heat treatment, the results of which will be presented in the next section

Figure 13. SEM sample mount system.

Bulk samples of each material were sent to Los Alamos after processing. Samples for corrosion testing at Los Alamos were coated with strips of TiN in order to prevent corrosion under a reference area. This coating was performed via pulsed laser deposition by Dr. Haiyan Wang. All samples were photographed, measured and documented before being sent to collaborators.

CHAPTER IV
EXPERIMENTAL RESULTS

Processing

The ECAE press load and die temperature were measured during the extrusion. Table 4 shows the maximum loads and temperature changes recorded for the samples. The extrusions were done in chronological order; a change in the tooling instrumentation between extrusions #18 and #20 involved moving the thermocouple from 2 cm away from the channel face and 2 cm from the top of the tool to 1cm away from the face and midway along the top channel. The first set, therefore, is representative of the change in temperature for a much larger volume of the die, whereas the second more closely reflects channel wall temperature. In the first thermocouple placement, the largest change in temperature was for billet #1, which was heated by resting in the inlet channel of the die for one hour prior to the extrusions. Note that this was the lowest temperature extrusion and required one of the highest loads to complete, indicating significant work that would lead to die heating. Billets #20 and #21 had loads and extrusion temperatures comparable to #3 and #4 so the differing temperature changes are approximations of the heating gradient for these extrusions. Figure 14 is a typical load/temperature curve for nickel-canned rods with the initial thermocouple placement. The first segment is the punch moving to meet the billet, then the load ramps up as the billet is compressed, upsets in the die and begins to flow around the corner. The load variations in the remaining portion correspond dimensionally to the nose, sample rods and plugs moving through the shear zone. However, this may be coincidental. The die temperature rises only slightly, despite the 400 C temperature difference between the billet and die at the

start of the extrusion as well as the heating from friction and deformation during extrusion. Figure 15 is a multipass load curve from billet #6. A high dislocation density is reached after the first extrusion causing increased but similar loads in the second and third passes. Note that the billet becomes shorter with each pass as a result of machining operations between extrusions.

Table 4. Die temperature changes in each extrusion.

Identifier	Max. Press Load (kips)	Temperature Change (C)
#1	264	10
#3	125	1
#4	153	3
#20	107	63
#21	172	88
#6	250	5
#10	291	1
#18	235	1

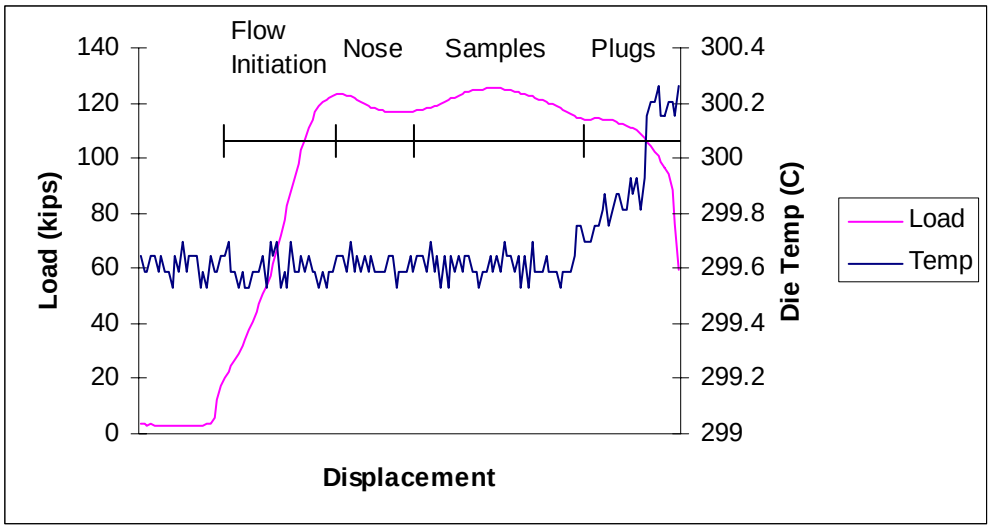

Figure 14. Press load and corresponding die temperature during extrusion of billet #3.

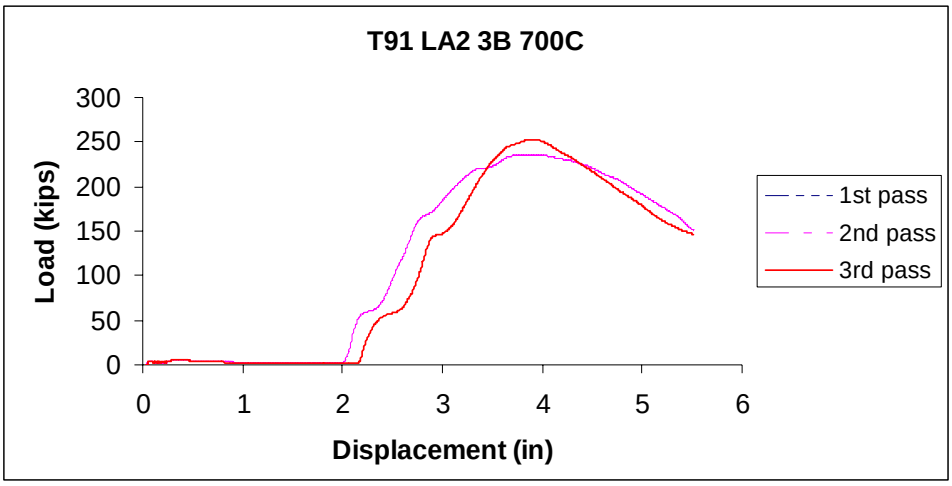

Figure 15. Multipass load curves during bare extrusion of billet #6.

Two of the billets, #10 and #18, shear localized during extrusion and did not produce viable samples. The load curve for #10 can be seen in Figure 16 while Figure 17 shows an image of the #10 billet. In this case shear localization was severe enough to cause fracture of the billet with enough force to eject pieces from the tool. Normally, loading would have ceased after the first spike but control problems to be discussed later allowed the extrusion to continue. Figure 18 is the load curve and Figure 19 a photograph of billet #18 where shear localization was the only major deformation mechanism but provided enough deformation to allow the billet to remain whole. These images can be compared to that of a typical extrusion such as #20 in Figure 20.

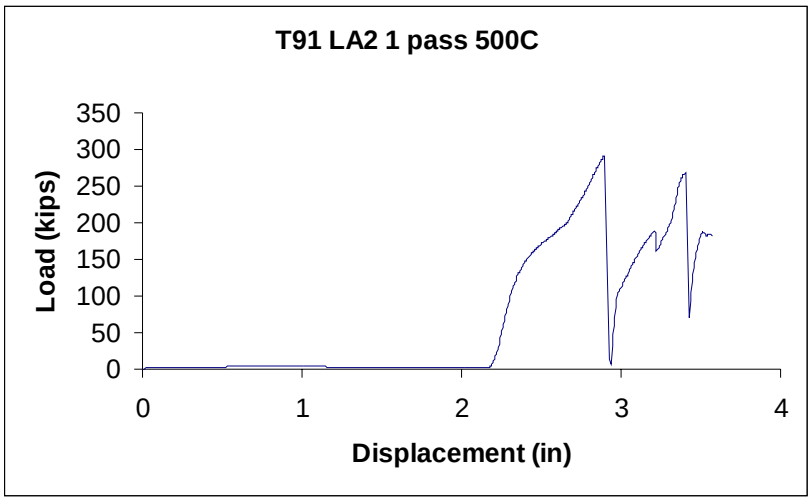

Figure 16. Press Load versus Displacement as #10 fractures during extrusion.

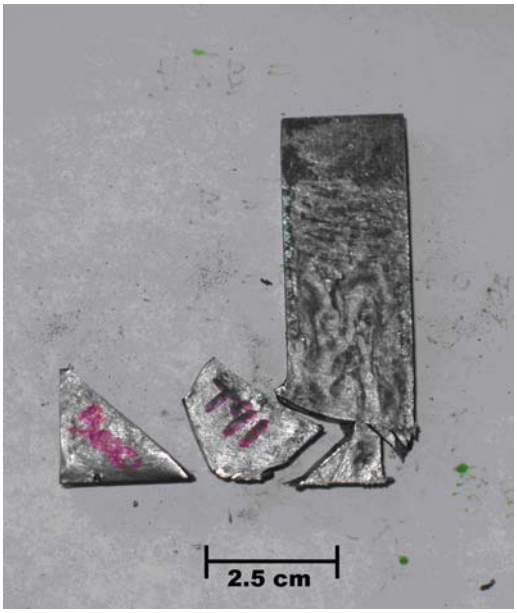

Figure 17. Image of partially extruded billet #10 with majority of fractured pieces, extruded at 500 C.

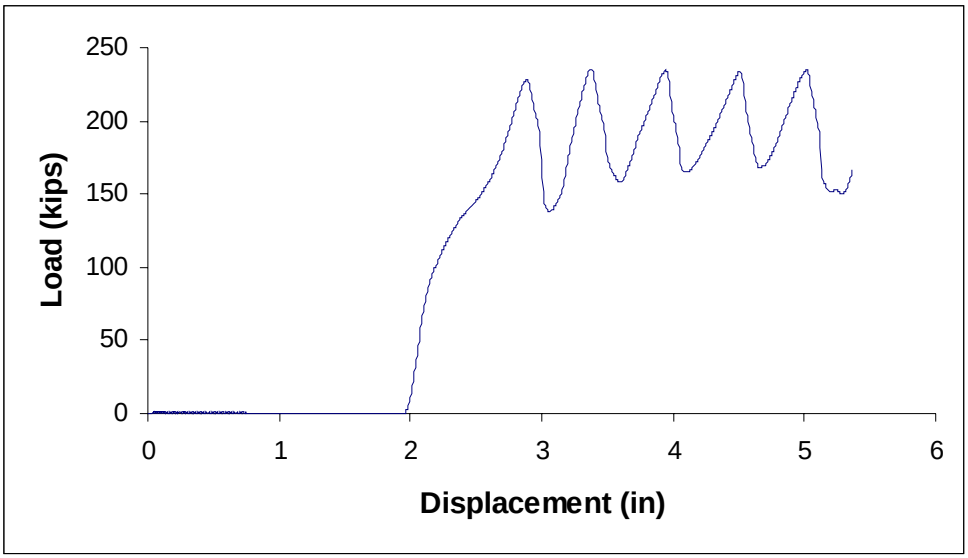

Figure 18. Press Load versus Displacement as # 18 shear localizes.

Figure 19. Image of billet #18 showing shear localization, processed at 600 C.

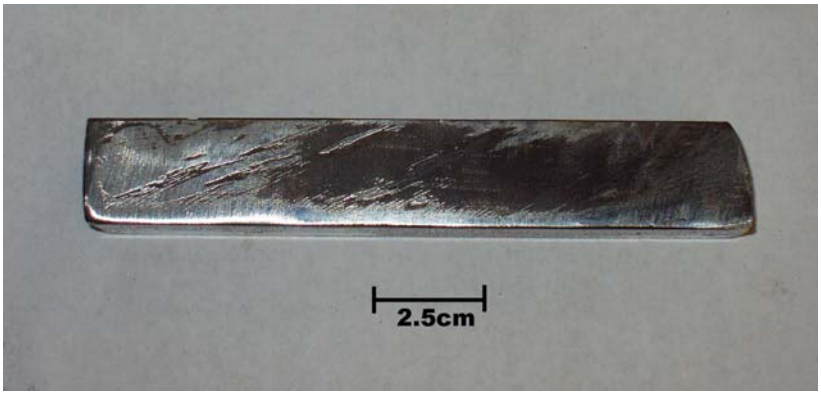

Figure 20. Image of #20, a typical successful extrusion, processed at 700 C.

X-Ray Diffraction

XRD was performed on all samples in order to check for any unexpected phases. No change was significant enough to be detected as can be seen in the 1AR and the 2AR based groups in Figures 21-23. The ά and Fe-Cr peaks are identified from d-spacing in the literature and power diffraction standards. The ά reference is Body Centered Tetragonal (BCT) martensite with some Body Centered Cubic (BCC) ferrite while the Fe-Cr phase is a BCC solid solution in which no supersaturation has occurred. The phases are difficult to distinguish because of the close proximity of diffraction peaks (the 110 peaks are separated by 0.1 degrees) and appear as unified peaks in most literature. The relative peak heights of 110, 200 and 211 differ, but this is to be expected since the processing would impart some texture and the samples from #1-4 were from the transverse plane, while the rest of the samples were from the flow plane. Any additional phases, such as the carbides or austenite that is sometimes present in small quantities, are below the approximately 5% threshold for x-ray detection. Some peak broadening occurs but it cannot be accurately used to estimate microstructural refinement at this level of

grain size. Additionally, the peak overlap of BCC and BCT phases might prevent this technique even with larger grain sizes.

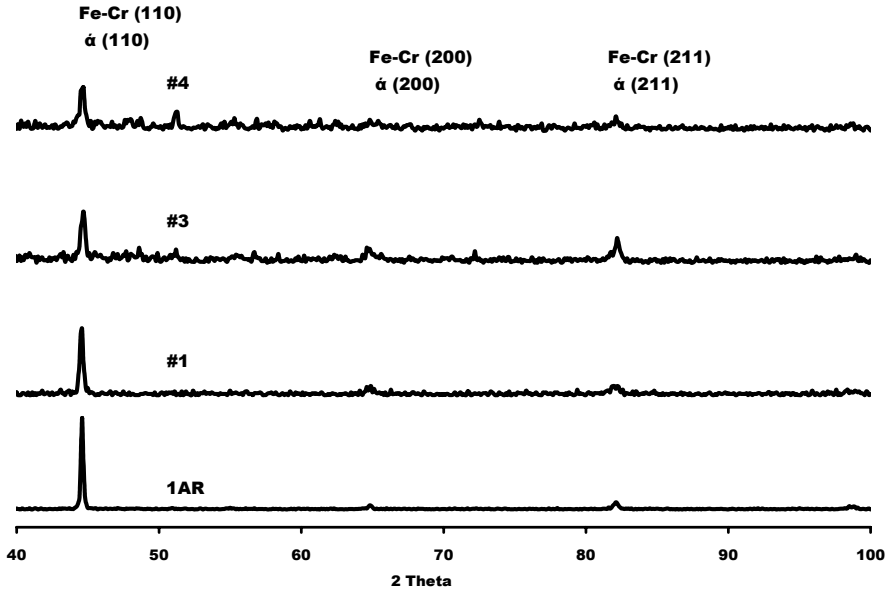

Figure 21. XRD of 1AR and #1-4 revealing major phases and the absence of austenite. Carbides and nitrides are not in a high enough concentration to be detected.

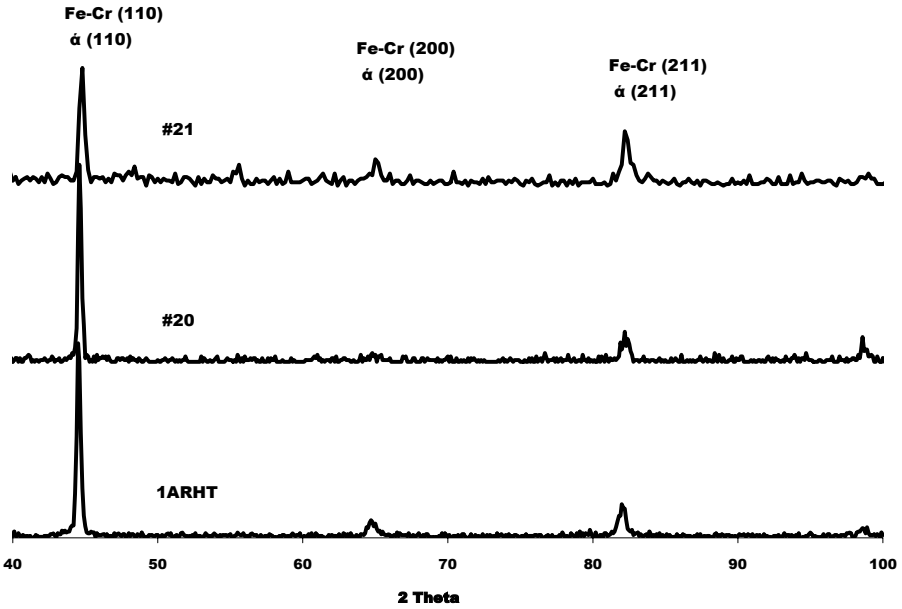

Figure 22. XRD of 1ARHT, #20 and #21. No austenite or other unexpected phases are present in significant quanitity.

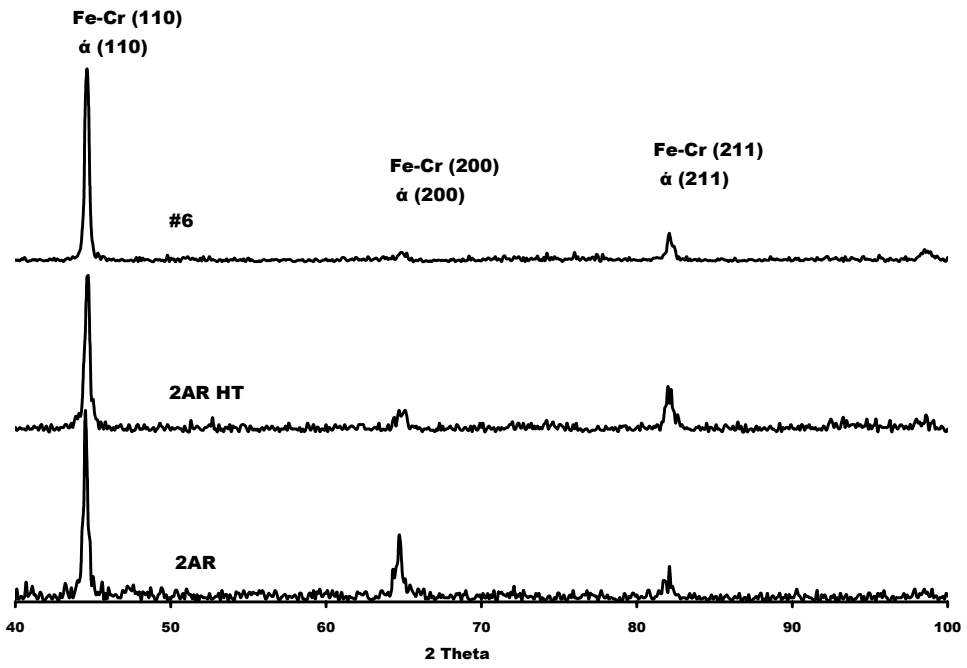

Figure 23. XRD plots of 2AR, #6, 2AR heat treated 1050C for 1 hour, vacuum cooled.

Transmission Electron Microscopy

Bright field TEM micrographs demonstrative of the sample microstructure are presented in Figures 24-32. TEM images of #1-4 are plane view of the transverse plane while the remaining samples are plane view of the flow plane. None of the samples had thin areas large enough to distinguish entire prior austenite grain boundaries such as the Figure 1 diagram. This was not surprising given the limitations of TEM and the lack of such an image in the literature. Diffraction patterns are included to indicate how strongly polycrystalline or textured each sample is. The diffraction aperture was selected to cover most of the pictured area, except in the case of Figure 33 where the pictured carbide took up the majority of the beam. The diffraction pattern for #1 (Figure 25) is nearly a continuous circle, indicating fine grains and random orientation, whereas the #21 diffraction pattern (Figure 30) shows a single strong pattern indicating highly preferred

orientation, despite the similar feature size. One would expect, therefore, that the boundaries of #1 would be a more significant barrier to dislocation motion than those of #21. These micrographs are from the same negatives used for feature size estimation. However, it should be noted that 1ARHT, #20 and #21 were so bimodal that a weighted average from two micrographs was used to estimate feature size. Figures 29 and 30 showing the microstructure for #20 and #21 illustrate the two typical morphologies.

The 1AR starting and processed materials were dominated by ferrite. As seen in Figures 24-27, the microstructural morphology was generally equiaxed and there was little evidence of martensite. The 1AR (Figure 24) material has a larger range of feature sizes than the processed materials. The large M23C6 carbides were observed in all four materials but in relatively small number compared to the 1ARHT and 2AR samples. Strong texture is observed in the 1AR (Figure 24) and #3 (Figure 26) materials. This should be expected for #3, a single-pass material, as ECAE imparts texture in many materials unless multiple passes are used to misorient the grains. Recrystalization may also be a factor in the LA1 materials processed at 700C, as will be discussed later.

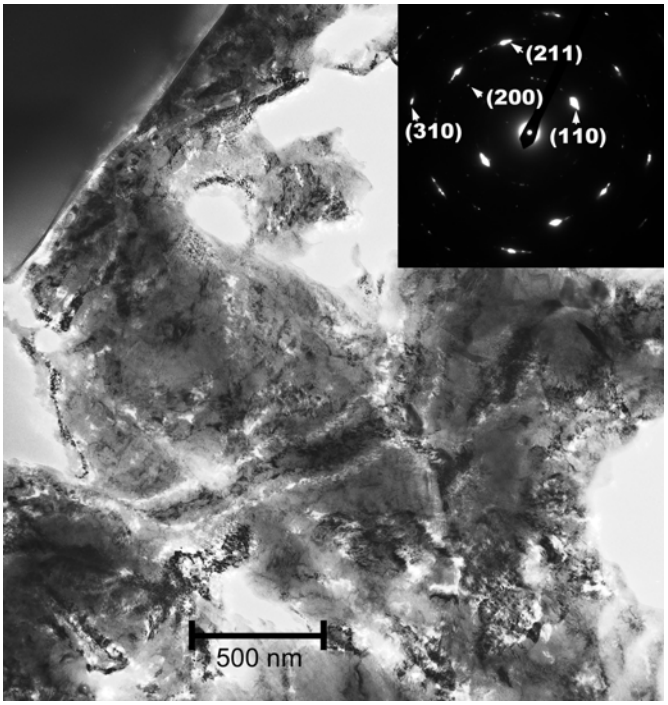

Figure 24. TEM micrograph of 1AR.

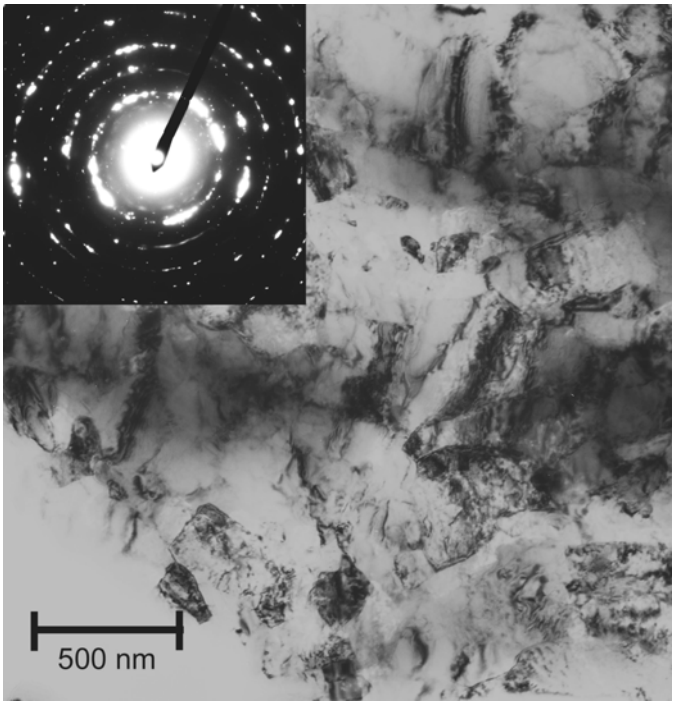

Figure 25. TEM image of #1.

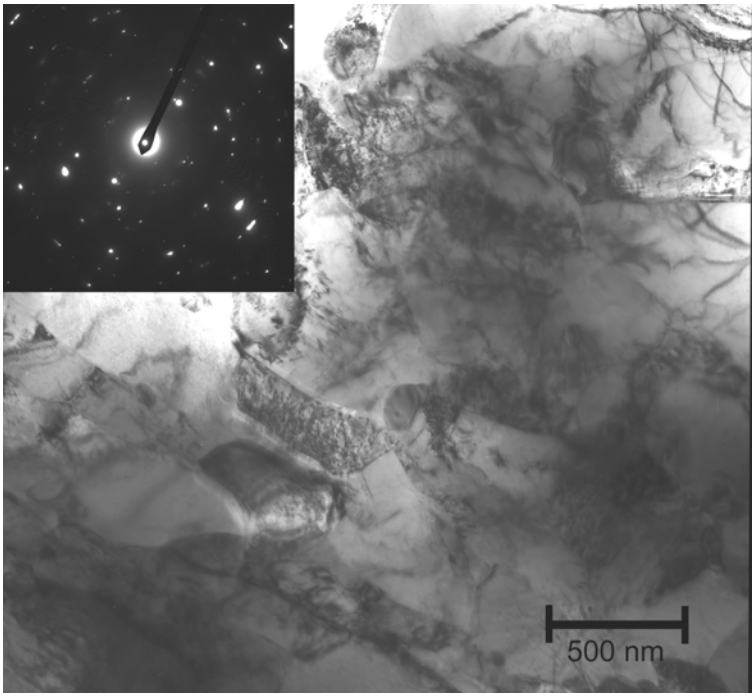

Figure 26. TEM image of #3.

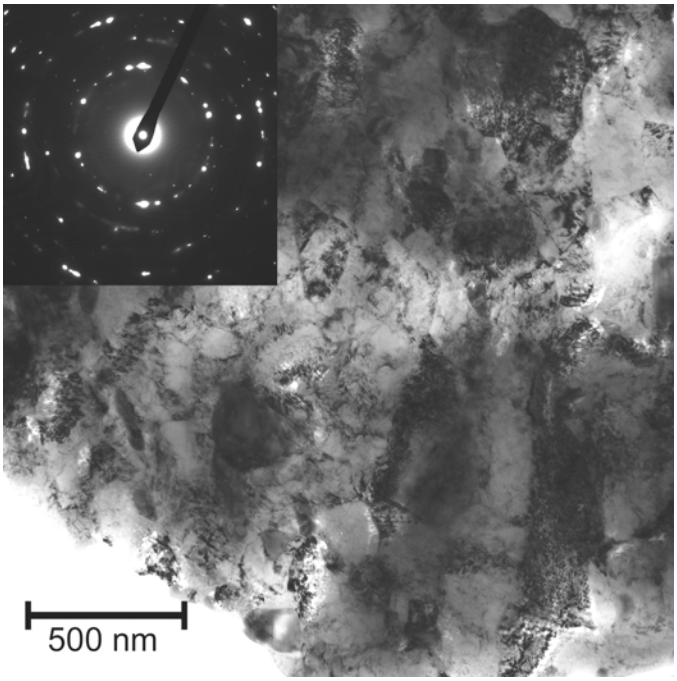

Figure 27. TEM image of #4.

The 1ARHT group is shown in Figures 28-30. The microstructure was fairly bimodal with thin areas dominated either by laths or more random ferrite. The 1ARHT material was especially dominated by long rectangular laths with a high concentration of precipitates or defects. In #20, these lathes dominated some regions, then seemed to pinch off where the microstructure turned into equiaxed ferrite. These ferrite regions could be of consistent feature size but many large grains were observed. Sample #21 was also bimodal in morphology but did not seem to have many large ferrite features. Some areas, like the one pictured, seemed to maintain traces of the lath structure after these laths were broken into smaller areas during ferrite formation. Few carbides were seen in 1ARHT but there was a notable increase in their number after processing. Many carbides were near, but not on, the grain boundaries in #20 and #21. Large carbides were rarely found outside of a boundary in the other materials.

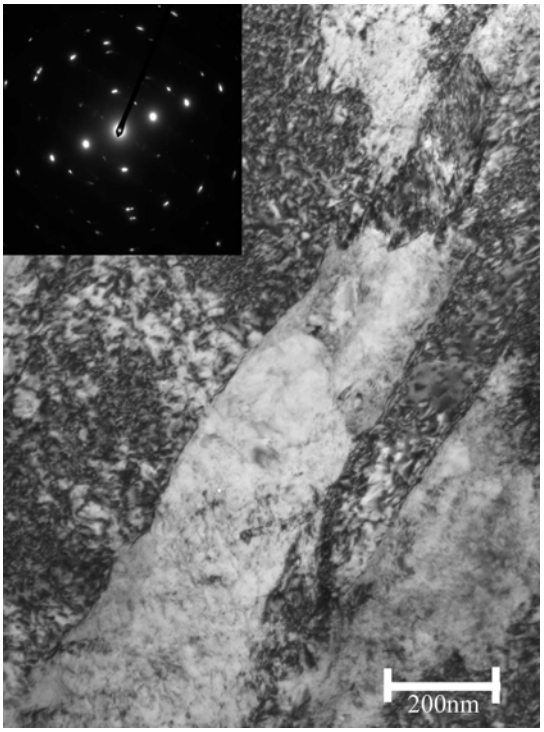

Figure 28. TEM image of 1ARHT.

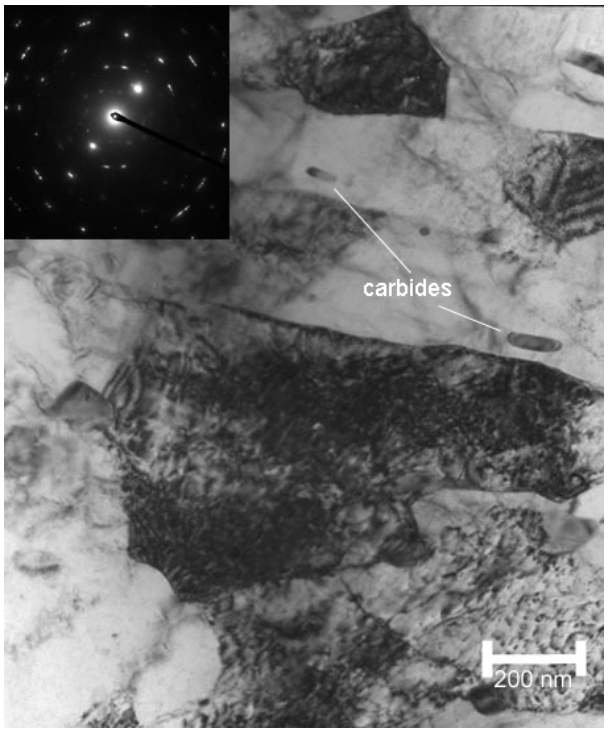

Figure 29. TEM image of #20.

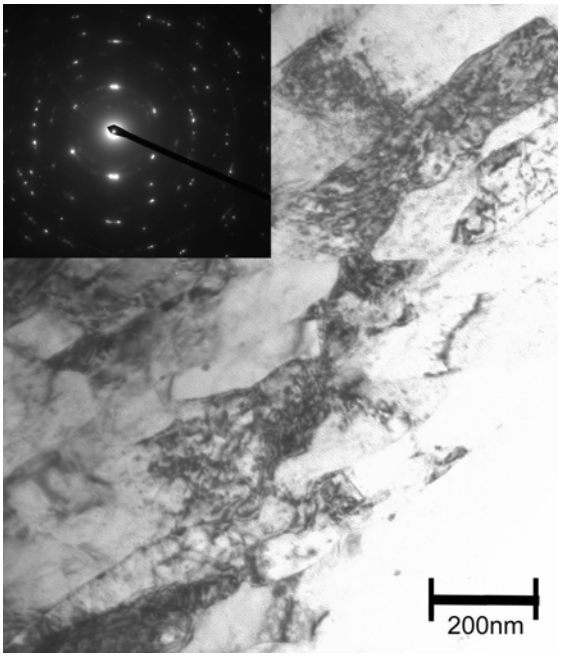

Figure 30. TEM image of #21

Figures 31 and 32 show the typical microstructure of 2AR and #6. The morphology of the 2AR material is somewhat random with an intermixture of sharp boundaries characteristic of martensite and more rounded ferrite boundaries, as opposed the 1ARHT materials where these morphologies dominate whole areas without intermixture. The number and typical size of visible carbides seemed to increase slightly after processing the 2AR material, which has more carbides than 1AR or 1ARHT. Rather than being randomly interspersed across the sample, most of the carbides in AR2 and #6 were found in clusters where carbides laced neighboring boundaries and were absent from surrounding boundaries until another cluster was encountered.

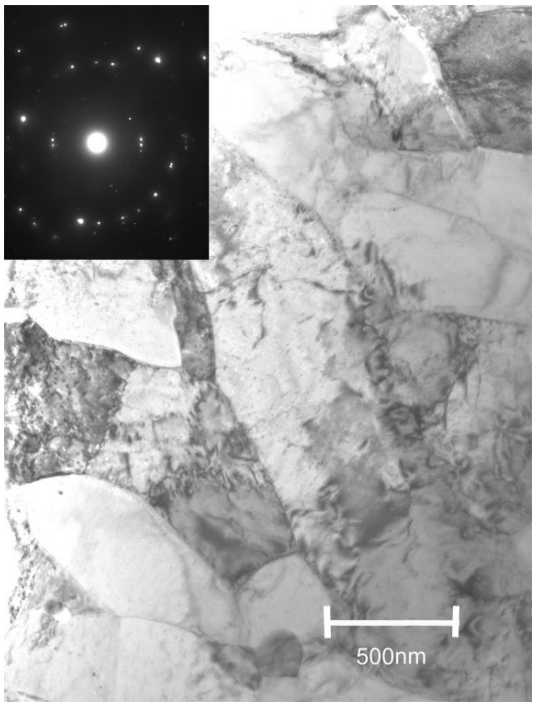

Figure 31. TEM micrograph of 2AR.

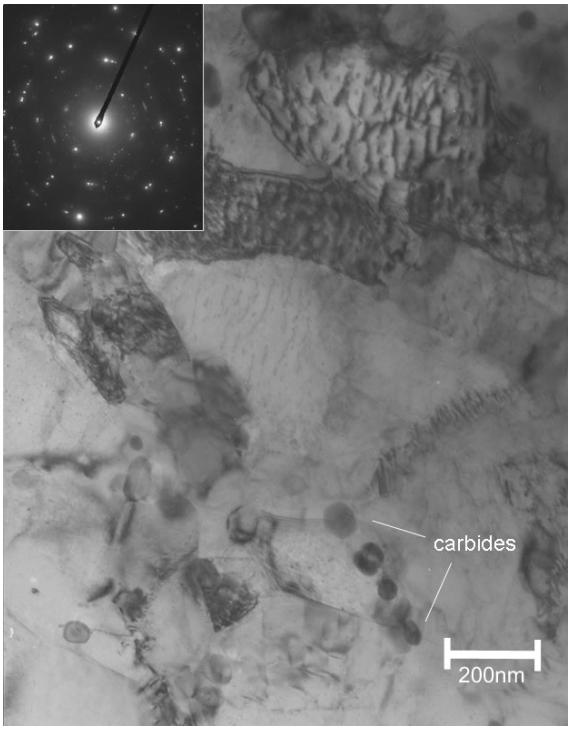

Figure 32. TEM image of #6.

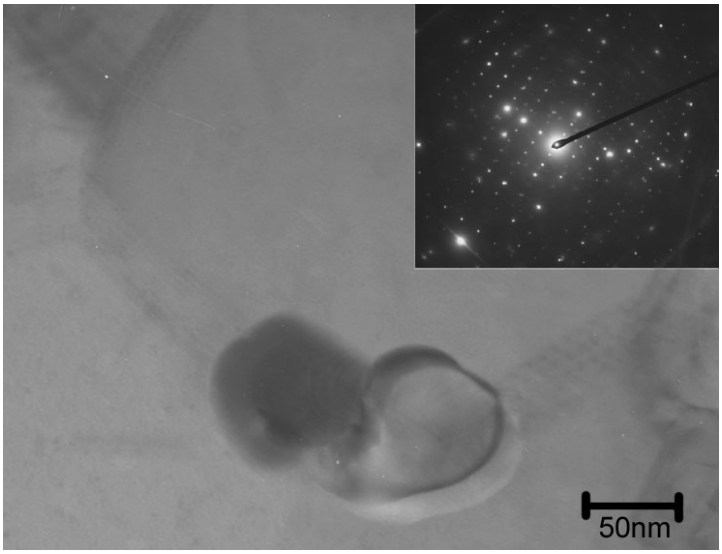

Figure 33. TEM image of particle in #6 with [112] diffraction from the carbide.

Feature size measurements are presented in Figures 34-36, grouped by starting material. The average feature size generally drops from 550 nm to 300-350 nm. The spread of feature size also decreases in most cases. The notable exception to both of these trends is #20, which remains at the higher average feature size and has a wider distribution than it started with. These trends and the major exception will be discussed further in the next chapter.

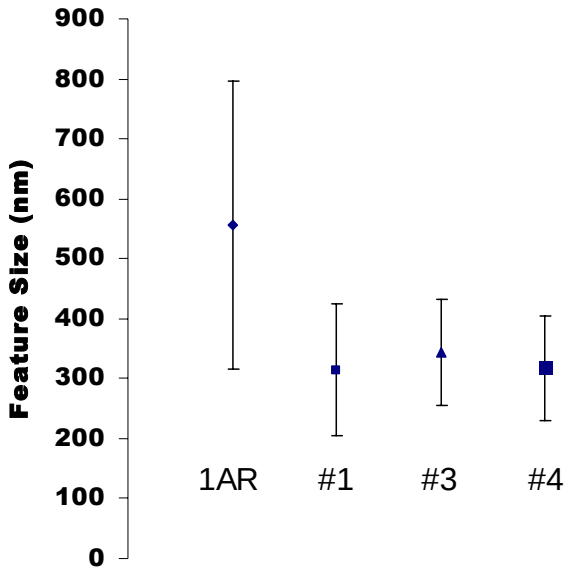

Figure 34. Feature size estimation of 1AR, #1, #3 and #4.

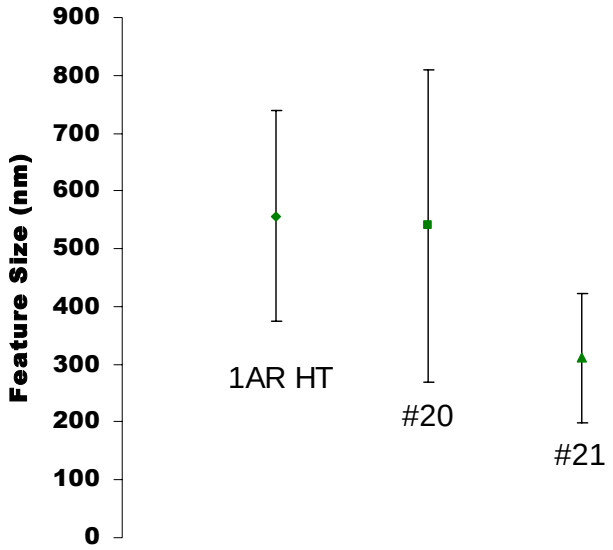

Figure 35. Feature size estimation of 1AR HT, #20 and #21.

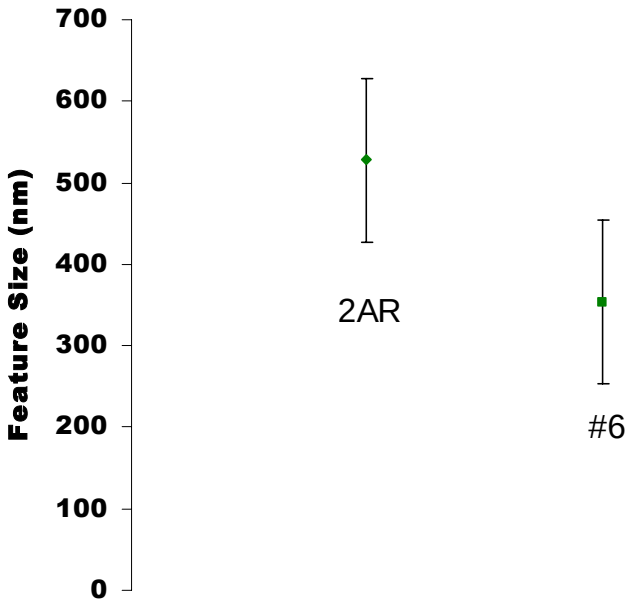

Figure 36. Feature size estimation of 2AR and #6.

Microhardness

An example of the impressions made with the Fischerscope is shown in Figure 37. This would be one of three grids on the same sample, ensuring that localized microstructure was not affecting the measurement. The need for this became apparent when large variations were determined to be real in such samples as 1AR and the heat treated 1AR. The modulus measurement capability of the Fischerscope was shown to be quite useful in this regard as discussed in the previous chapter.

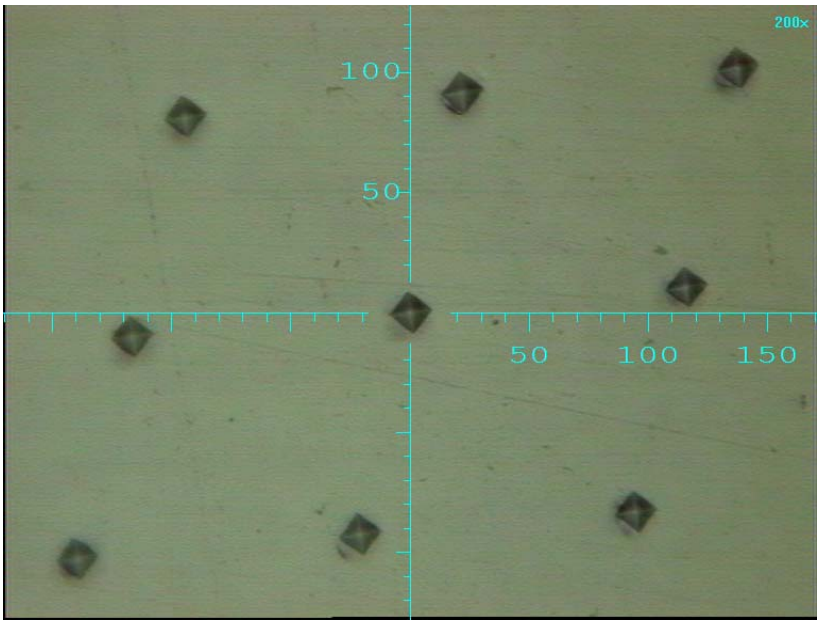

Figure 37. Indents on #1with scale in microns.

Figure 38 summarizes the affect of processing temperature on material hardness; there is little correlation. However, a few notable comparisons can be made. The three starting materials and their processed counterparts are distinguished by color. The 1AR material hardens with processing as expected. Samples #1 and #4, the two-pass materials, are the hardest of this group which makes sense from a defect accumulation

and grain refinement perspective. However, the #3 microstructure is only slightly more course as seen in Figures 34 and 39.

The 2AR and 1ARHT materials tell a different story. Their softening indicates that the tempering effect of bringing the samples to temperature for one hour before extrusion was significant. Although this was not anticipated at the time of the work, the heat treatment considerations discussed in the literature review indicate that this tempering should be expected. The 1AR and 1ARHT materials that underwent equivalent processing in #4 and #21 differ significantly in hardness, indicating that the hardening effect of martensite and precipitation remains after processing.

Figure 39 illustrates the hardness versus estimated feature size. The feature size distribution is quite bimodal with a strong correlation to imparted strain. However, there is no similar bimodal distribution of hardness. The 1AR material, in which martensite is essentially absent, is the only set with the typical ECAE trend of increasing hardness with decreasing feature size.

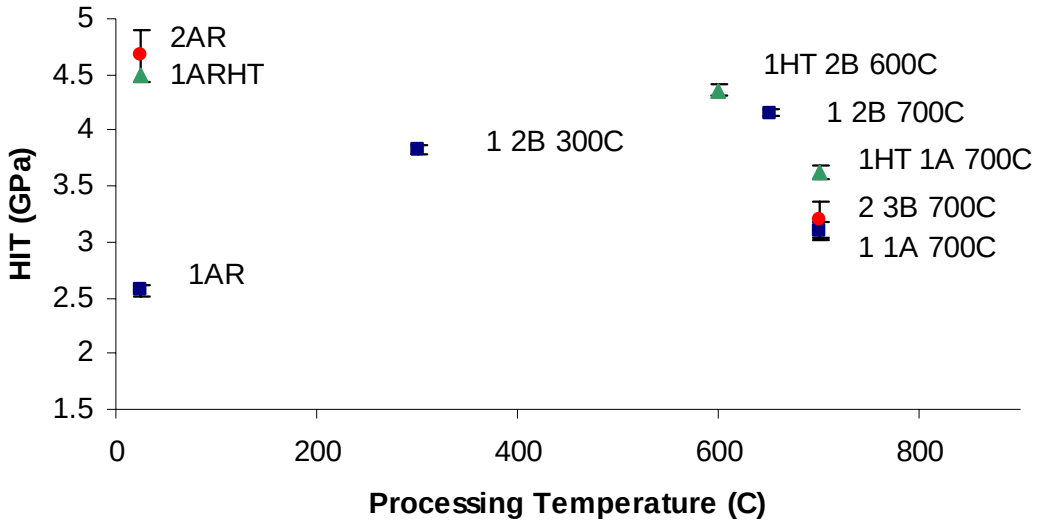

Figure 38. Hardness versus processing temperature of studied materials.

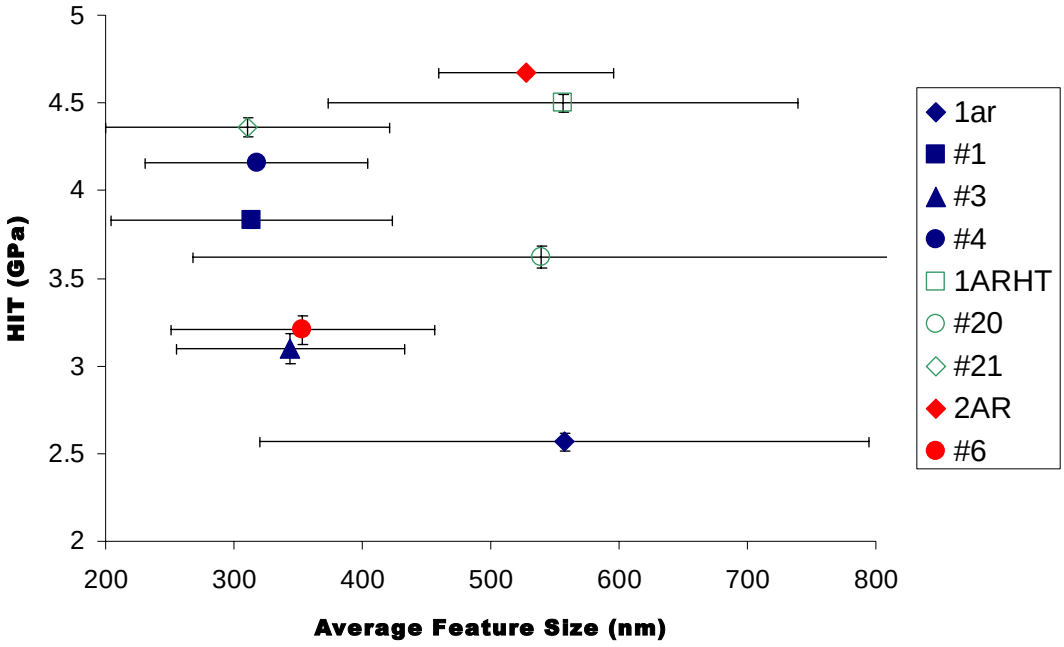

Figure 39. Hardness vs. estimated feature size. Feature size estimated from limited information and error bars indicate deviation over the examined areas.

Tensile Testing

Tensile testing was limited to two samples per material. 1ARHT and #20 were limited to one sample due to improper mounting while EDM cutting the samples, resulting in an unusable coupon with varied thickness. Figure 40 summarizes the results from the 1ARHT group. Sample 1AR and the higher temperature single pass sample #20 exhibit modest and comparable ductility. Sample #20 was therefore significantly strengthened by heat treatment and processing without a penalty in ductility. Sample 1ARHT has a Total Elongation (TE) similar to the lower temperature, two pass #21 and a slightly higher Ultimate Tensile Strength (UTS). However, the 1ARHT engineering stress begins to drop much more quickly than #21 due to more significant necking, confirmed by sample inspection. This indicates that the true stress would be much higher for 1ARHT than #21.

Figure 41 shows the more limited 2AR set. Sample #6 has significant varation between the two samples but is comparable in strength and ductility to #20 as one of the #6 curves nearly overlays the #20 curve. These materials started with similar strength before being processed at the same temperature, indicating that tempering during processing preparation may be more significant than the imparted strain. This is especially notable since #6 received three times the strain. Spending one hour in the furnace at 700C prior to each additional pass may have reduced the impact of prior strain on #6. As mentioned, 2AR is comparable in strength to 1ARHT but has roughly half the ductility and no noticeable necking in the samples.

Modified 9Cr-1Mo in the typically desired tempered condition has a UTS of approximately 650-700MPa, near the 1AR level. However, the corresponding TE in the literature is 20-25%, far more than the 1AR material [32, 85]. Even #6, with the highest average elongation, falls significantly short of this level as seen in Figure 41. Strain rate was not varied and literature values are not reported with rates. However, tensile tests were conducted in a deliberate quasi-static manner to avoid strain rate affects. Table 5 summarizes Ultimate Tensile Strength (UTS), Young's modulus (E), Yield Strength (YS) and Total Elongation (TE) for these tensile pulls with averages where applicable. Most notable among these results besides the findings that are more obvious in the previously discussed figures are the modulus and yield strength values. Literature values for T91 are around 210 GPa with a 550-600 MPa YS for the tempered material. The YS values here are by comparison clearly low with #6 as the only exception. This is partly due to the widely varying modulus values, which are used to calculate the 0.02% offset for yield strength.

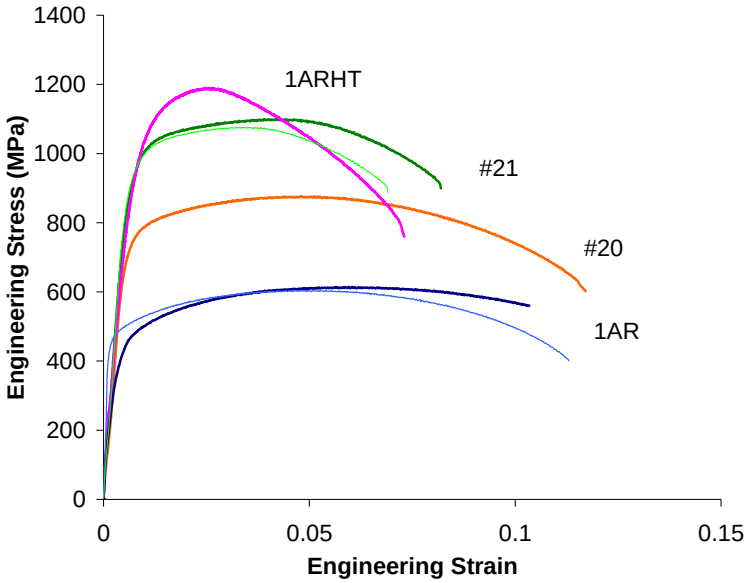

Figure 40. Raw data of 1AR based tensile runs.

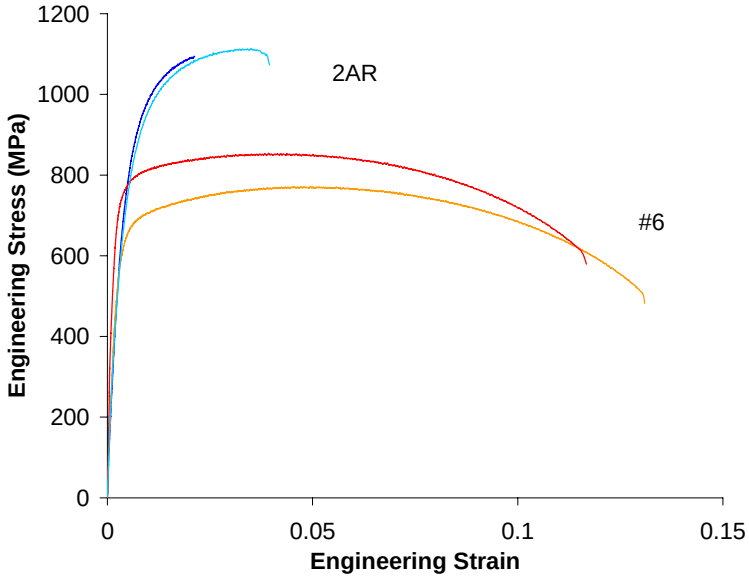

Figure 41. Raw data of 2AR based tensile runs.

Table 5. Results of tensile testing.

Material	1AR	1ARHT	#20	#21	2AR	#6
Processing	x	Heat Treat	1A 700 C	2B 600 C	x	3B 700 C
UTS (MPa)	609	1190	877	1090	1101	814
E (GPa)	213	134	136	155	217	266
YS (MPa)	236	52	445	116	316	653

Tensile fracture surface images were taken for 2AR and #6 via SEM. Figures 42-47 show several magnifications of each. Comparing Figures 42 and 45 illustrates the large difference in necking behavior after processing. The 2AR sample in Figure 42 has large faceted surfaces in the left half while smaller but still obviously brittle features dominate the right. Figure 43 shows a closer look that appears to indicate localized melting. A lone particle rests in a small crater on the surface. Figure 44 zooms in on a second, similar particle found elsewhere on the surface which is more imbedded in the surrounding material. The two morphologies of localized melting in this sample meet in this figure and can be seen more clearly than in the wider views of Figures 42 and 43. The long, ridge-like features cover the majority of the sample while the smaller puddle-like features also show up on a significant fraction of the surface.

In addition to the necking of #6, Figure 45 shows that a few small areas of the sample held together and drew out farther than the majority of the sample. This was noticed during testing both samples, as the snap of a typical break was heard but 100-200 MPa of engineering stress still registered briefly before complete failure occurred. Upon closer inspection in Figure 46, deep pitting and pullout can be seen over the sample. Long fissures like the one pictured were seen in several locations. However, the more dominant features are the round pits covering the surface. Figure 47 reveals that many of these deep pits contain 2-5 um spheres like the few seen across the 2AR sample.

Electron Dispersion Spectroscopy (EDS) mapping was inconclusive as to their makeup, although simple EDS on an area dominated by two particles hints that they have a significant Si content.

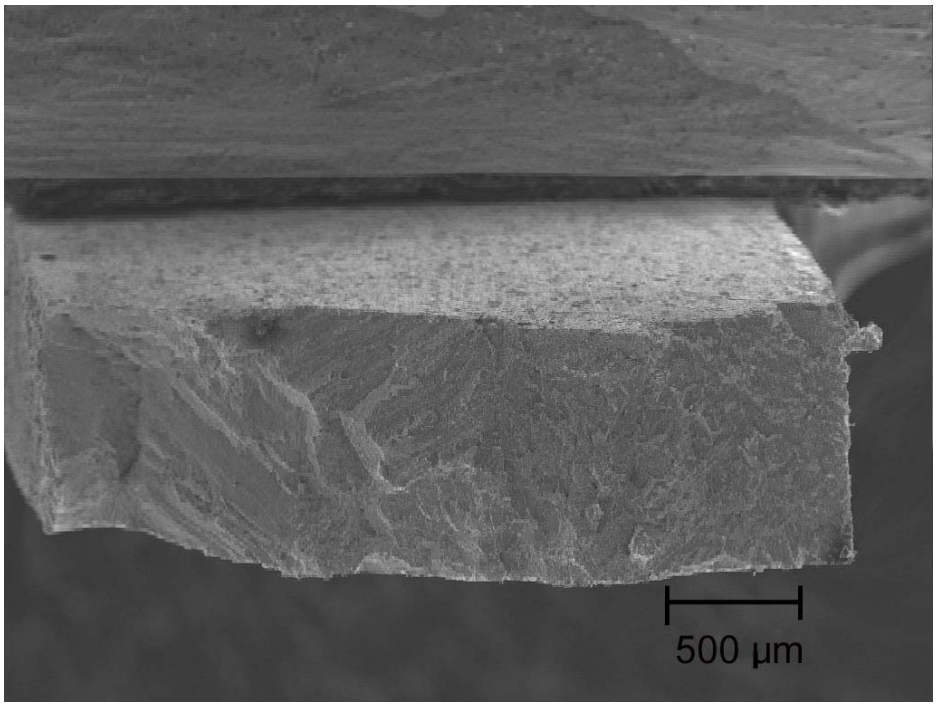

Figure 42. SEM fracture surface image of 2AR 25X.

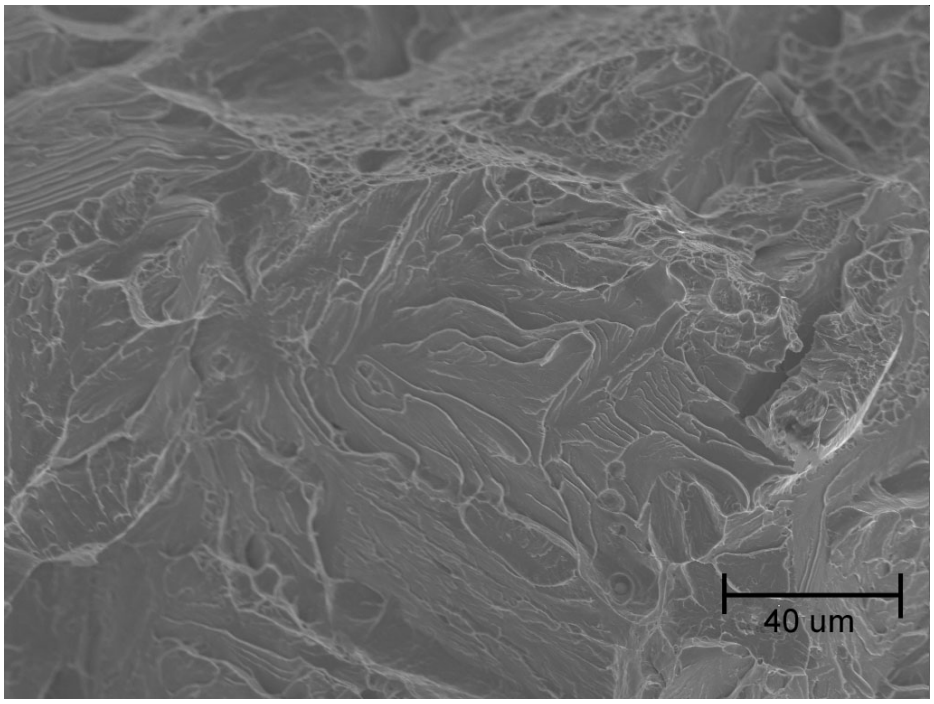

Figure 43. SEM fracture surface image of 2AR 600X.

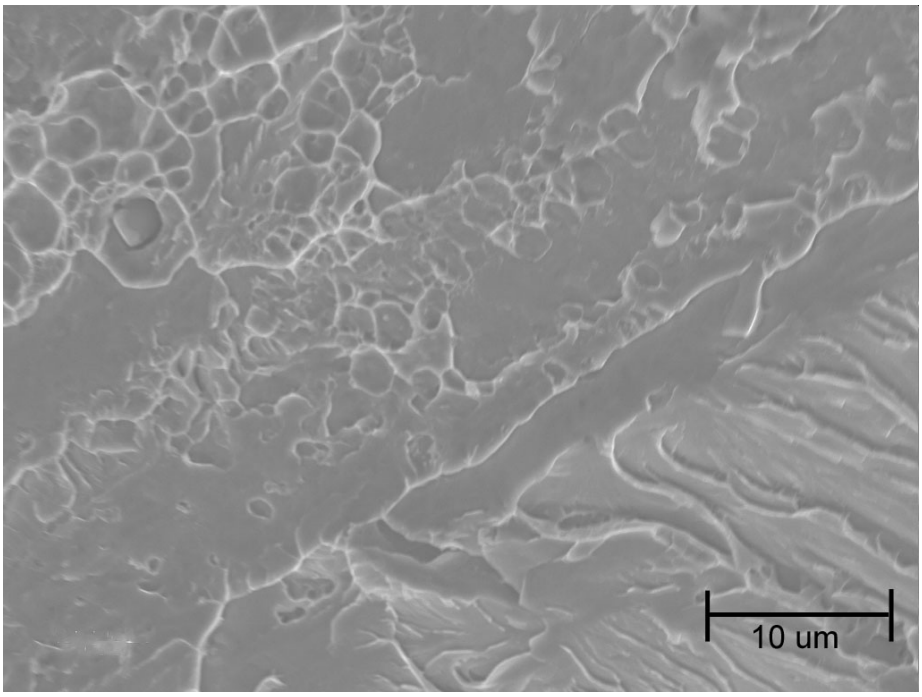

Figure 44. SEM fracture surface image of 2AR 2500X.

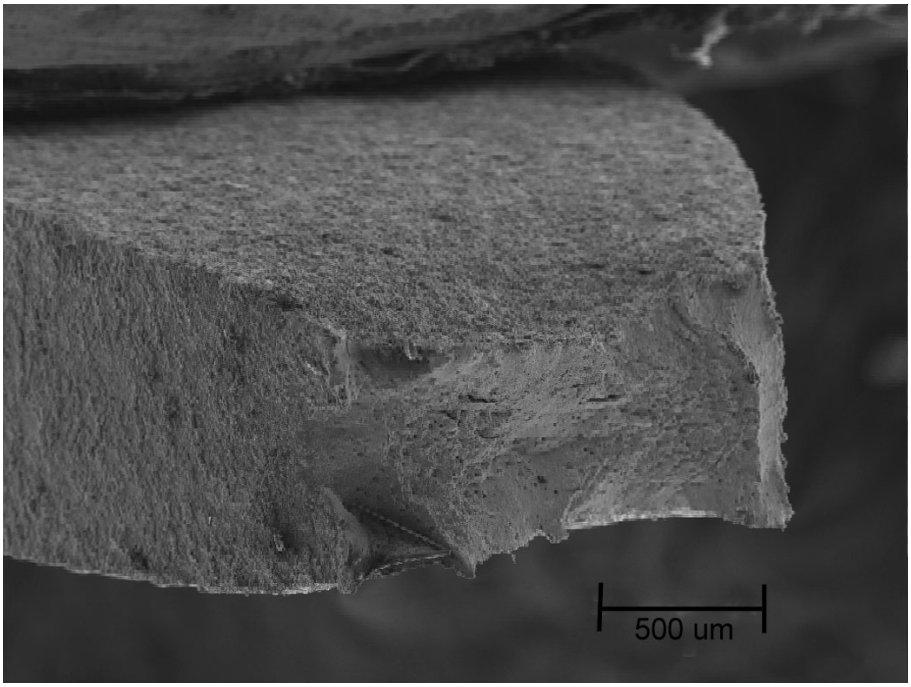

Figure 45. SEM fracture surface image of #6 45X.

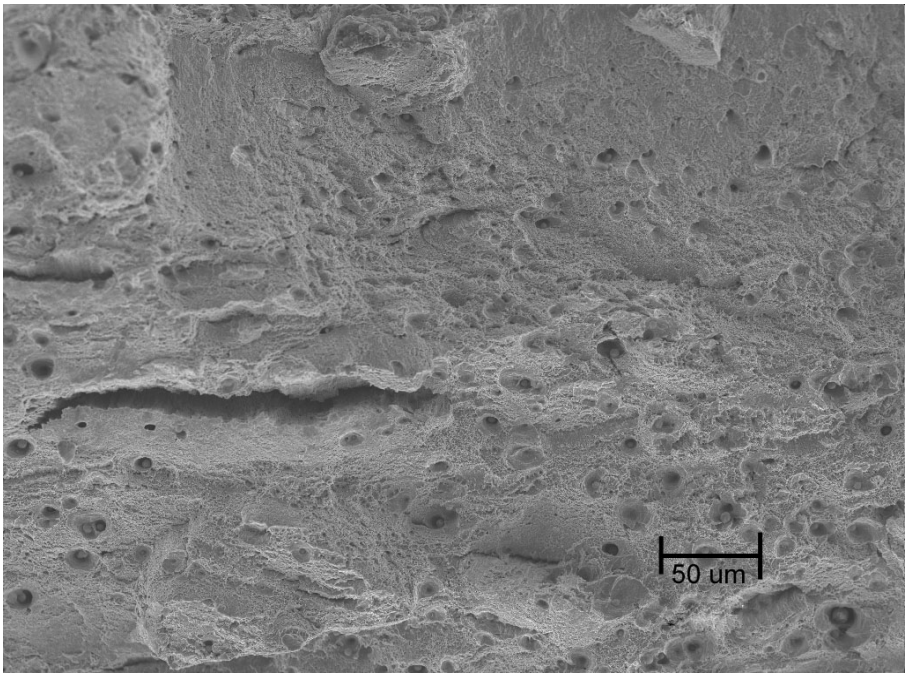

Figure 46. SEM fracture surface image of #6 270X.

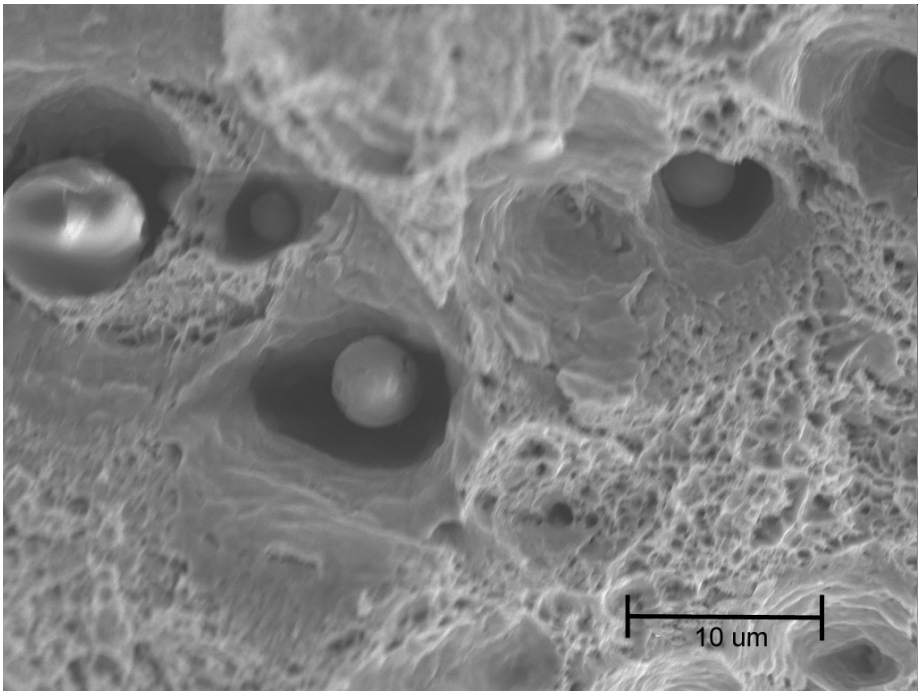

Figure 47. SEM fracture surface image of #6 2700X.

Heat Treatment

Annealing curves from some of the 1AR-based samples are shown in Figure 48. Once again, limited sample volume prevented the inclusion of #1-4 in the annealing study. Sample 2AR has a significantly higher softening point and is included as a comparison to illustrate the effects of chemical composition and the resulting precipitation, delaying the softening point by approximately 100 C. The other materials all soften most significantly between 700 C and 800 C, the tempering range given for this material. The 1AR material shows no significant softening as it is nearly all ferrite before heat treatment. The other materials, dominated by martensite phase initially, soften as a result of a phase transition to ferrite. Additionally, the fine precipitates dissolve in this temperature range. At 900 C, martensite will begin to re-form during cooling. The processed materials, #20 and #21, have a stronger drop in hardness than 1ARHT. All

1AR materials have at least a somewhat higher hardness after a 900C heat treatment than they started with, even including the previously heat treated 1ARHT. Not shown in this figure is that 2AR climbs to within 5% of its starting hardness when heat treated at 1050C under the same conditions.

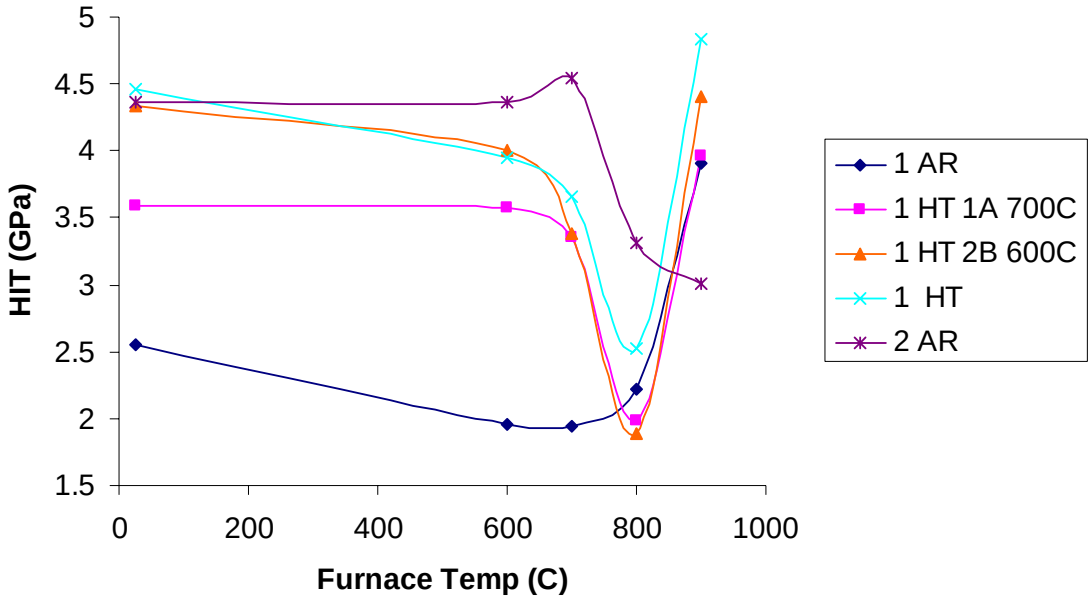

Figure 48. One hour annealing curve for 1AR, 1ARHT, #20, #21 and 2AR.

Ten hour vacuum heat treatments were performed on #1-4 using material sent to LANL soon after this batch was processed. The hardness of these samples can be seen in Figure 49. Although they do not reach beyond 700C, the softening behavior appears similar to #20 and #21. Optical microscopy was also performed on etched samples after annealing. The data and images are included as Figures 50-55. The etching was unable to reveal boundaries in #1 before heat treatment. However, the prior austenite boundaries were revealed in the other cases. Despite the difference in size and boundary type, morphology carries over between the TEM and optical images with the exception that

texture in #3 is visible in the morphology rather than simply a diffraction pattern. This texture is strong enough to remain even after grain growth. Grain growth can clearly be seen in all samples after ten hours at 700C with the two-pass materials reaching roughly the same fine but visible size and #3 growing to tens of microns.

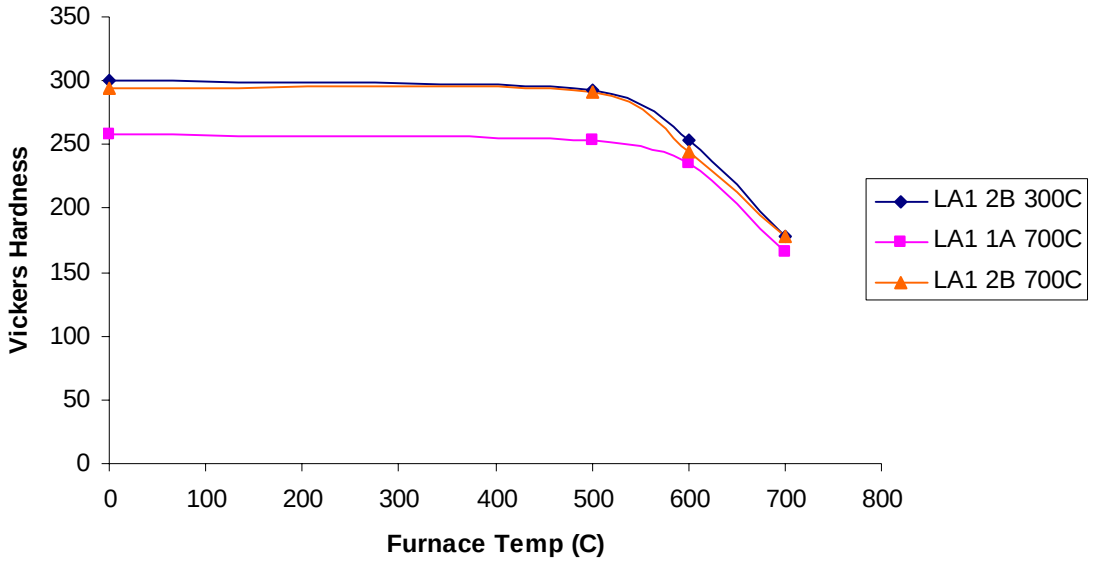

Figure 49. Ten hour annealing curve for samples #1-4.

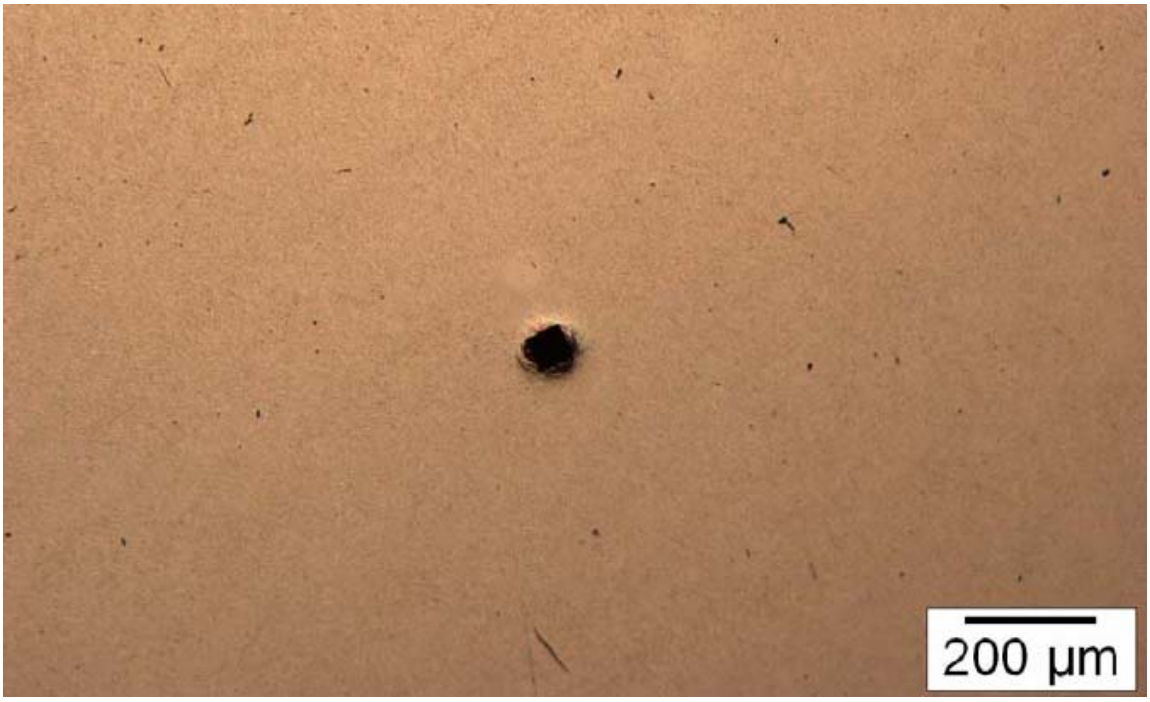

Figures 50. Optical Image of #1 from Peter Hoseman.

Figures 51. Optical Image of #1 700C HT from Peter Hoseman.

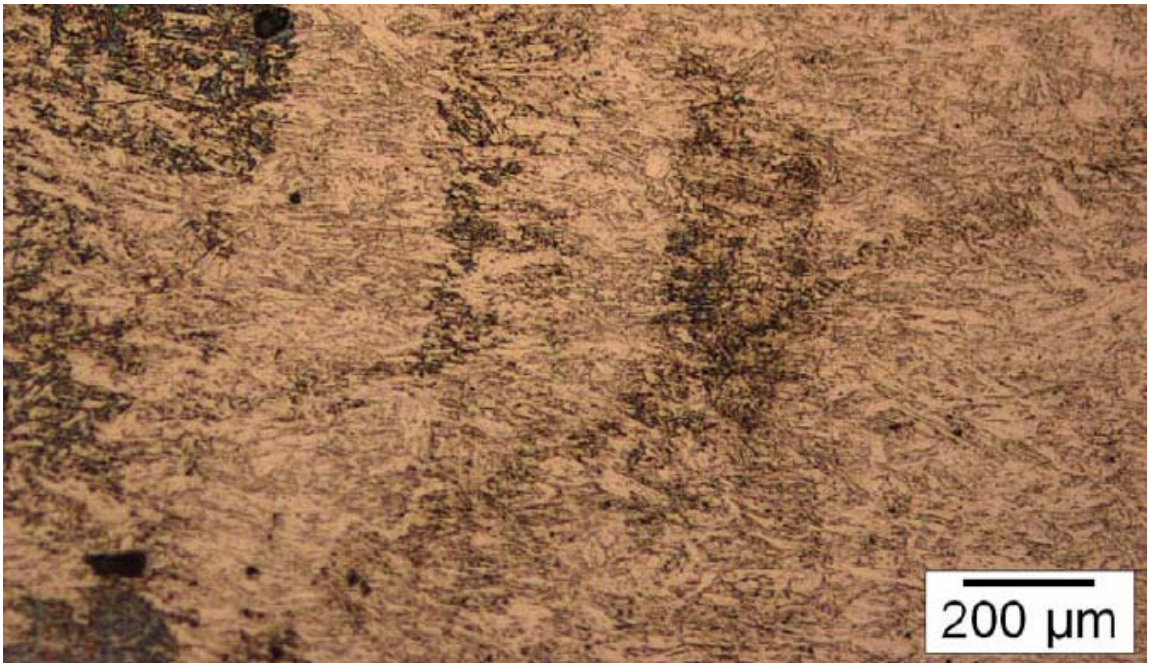

Figures 52. Optical Image of #3 from Peter Hoseman.

Figures 53. Optical Image of #3 700C HT from Peter Hoseman.

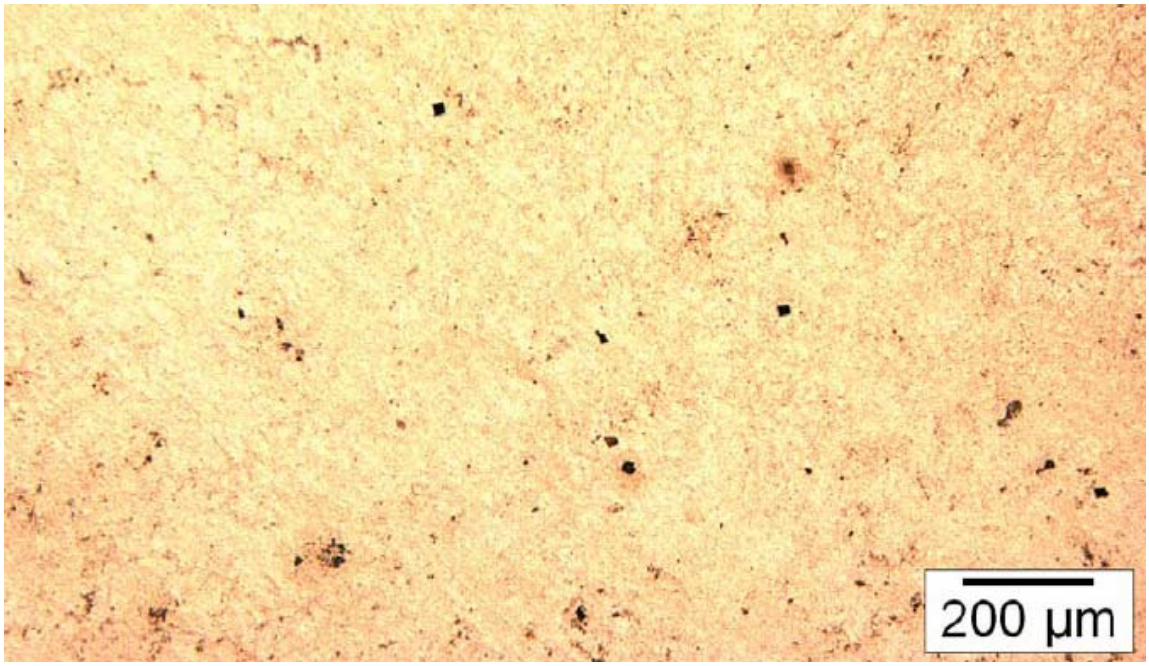

Figures 54. Optical Image of #4 from Peter Hoseman.

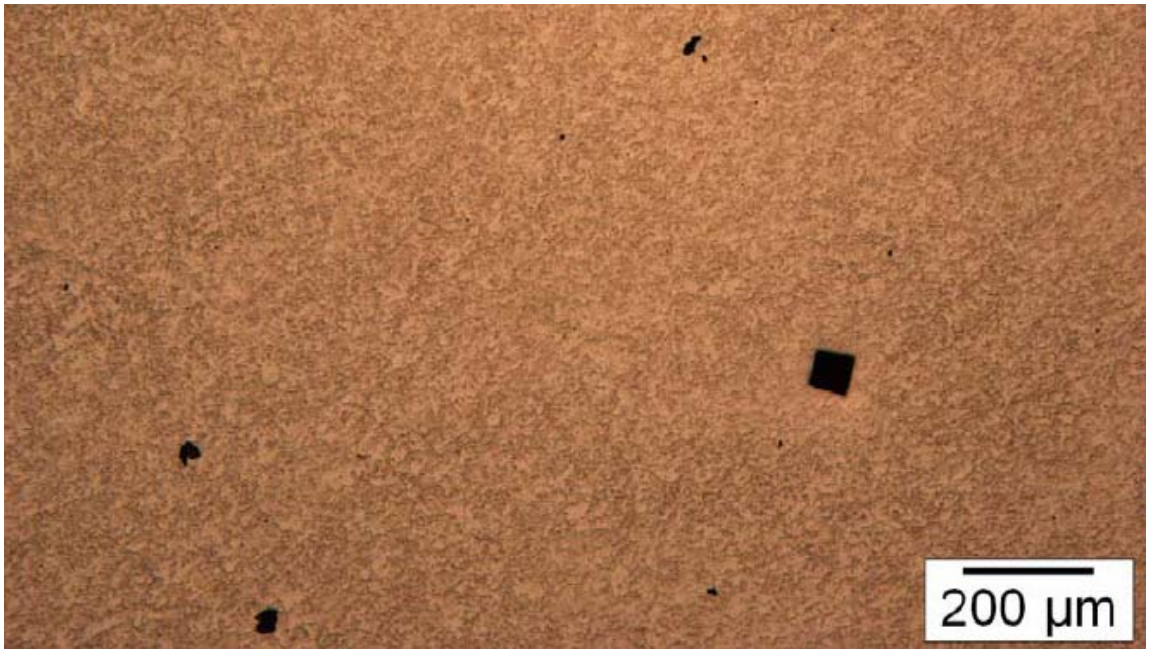

Figures 55. Optical Image of #4 700C HT from Peter Hoseman.

CHAPTER V
DISCUSSION

Starting Material

Despite the commercial nature of this alloy, materials for this study were obtained from Los Alamos from small batch suppliers as custom heats. This likely had a great deal to do with the as-received condition of the samples, especially the LA2 batch. The thick scale of oxides around the as-received block of LA2 material indicate that it was improperly cooled and the particles revealed on the tensile fracture surfaces call some of the chemistry and homogeneity into question.

During the process of EDM cutting the LA2 material, it became apparent that there was a high concentration of oxides to approximately ¾ cm inward from the sides. Given the deep pitting and rust around the sides, this was not surprising but it did indicate that the material was exposed to oxygen at high temperature for a significant time period. The chemistry of the sample near the core is known from a recent hydrogen flame chromatography test commissioned by collaborators at Los Alamos. However, chemistry closer to the edges may have been affected.

ECAE

While it is fundamentally a simple process, problems that arise with ECAE can be frustrating. The system is controlled through an MTS supplied MS Windows application which can result in errors due to errant mouse or keyboard input. However the system is capable of controlling the press with a good deal of accuracy and can ensure a safe working environment if programmed and operated correctly. Nevertheless, safety switch

failures, inertia and other problems make basic mechanical safety features like blowout valves and a Lexan safety shield necessary and useful.

Extrusion of the 1AR rods had mixed results. The load and temperature curves for the first round of extrusions showed no shear localization and indicated generally smooth flow around the die corner. However, most of the rods partially shifted off of their stainless steel plugs during extrusion so processing was incomplete and uneven. #1 seems to have tilted against the plug during both extrusions. #3 seems to have extruded well, having a flat and clean face against the plug. #4 shifted off of the plug, probably during the first extrusion. Unfortunately, due to the small sample volume and the need to prepare samples for several different experiments, variability in the microstructure could not be properly quantified.

The 1ARHT extrusions went quite well. Extrusion loads were small in part due to a recent rebuild of the die as well as improved lubrication over the 1AR extrusions. Shifting within the nickel can seems to have been minimal. Further, this second set of extrusions leveraged the EDM recently acquired in order to create large samples with useful geometry from relatively little available starting material. This enabled investigation of more properties than the first set of extrusions and was the primary motivator for additional extrusions with LA1 material.

Difficulties were encountered with the LA2 extrusions as well as other stainless materials processed at the same time. Originally, the operators coated billets with boron nitride aerosol spray lubricant. However, this proved inadequate and the stainless samples and cans were microwelding to the front and back legs during extrusion. This problem was not obvious until failure occurred since the increasing loads from

roughening faces were being observed while changing materials between extrusions. Failure occurred when the load limits of the tooling were exceeded and the front leg was driven into the base. Additional material was welded onto the base and it was milled back to specification. The tool was pressed back together with the appropriate shim thicknesses in various locations to bring the channel back into specification and extrusions were continued. However, these extrusions were thereafter carried out with the Deltaglaze glass lubricant. It was discovered that this was the lubricant with least friction at temperatures as low as 500 C, below the quoted temperature range. However, it is not known if the surface damage to the tooling caused by hard glass at this temperature is significant compared to other alternatives. The only known downside to this lubricant is that it requires a thoroughly clean and slightly rough surface to adhere, and all but a thin layer will pool at the bottom of the billet while heating in the furnace, which can make rapid insertion into the die problematic.

Temperature control is a concern with all of the extrusions. In the case of #1, the billet and die started the extrusion at an essentially uniform temperature. However, the rapid plastic deformation of a strong material generates a great deal of heat. The 10 C temperature rise at the thermocouple indicates that this heating would be significant in the billet, although it would not have reached the martensite start temperature around 400 C. In the case of the other, higher temperature extrusions, this deformation heating is offset by quenching from contact with the die. The tool cannot be operated above 300 C as the strength of the steel starts to drop noticeably. This would prevent successful extrusion of some of the more difficult, high load samples and would not perform well at 700 C even with relatively mild loads. The higher temperature extrusions, therefore, had

competing effects of die quenching and deformation heating influencing the billet temperature. Since the high temperature extrusions are intended to be performed at temperatures just under recrystallization, this temperature uncertainty is a concern. Additionally, the mechanical energy being added to the system may lower the required temperature for recrystalization. From the results, it appears that #20 may have experienced significant dynamic recrystalization, as its average feature size is much larger than other processed materials, even that of the similar #3. Additionally, the variation in feature size is larger than the other processed samples, which would be expected when recrystalization conditions are barely being met.

TEM

Quality of the TEM samples increased dramatically after the switch from a conventional ion miller for 1AR and #1-4 to the PIPS system. The more tightly controlled beam and stable current supply helped to create wider thin sections for viewing. Obtaining representative TEM micrographs was a difficult task in many of the samples. The small thinned area of the samples meant that the field of view was restricted to a few microns at best, smaller than the typical prior austenite grains. However, using multiple images and attempting to find at least one representative area suffices for this work.

The feature size estimates generated from TEM figures and corresponding hardness values do not agree well with the Hall-Petch relationship, indicating that the affect of these boundaries on strength is not significant compared to precipitation and other defect accumulation. Of course, since feature size was typically reduced by only

one third and the annealing curve demonstrates that heat treatment is capable of more than doubling the material hardness, this is not surprising.

According to ASTM standards, grain size should be estimated from images in which at least 50 grain boundaries can be counted with each line. This method results in an accurate measurement of grain size. It is unfortunate that the measurements in this thesis could not be performed on large areas such as this. Typical measurements used 6 to 12 intercepts per line, adding to the problem of bias in image selection. Additionally, TEM images, unlike SEM or optical, reveal a level of detail for which this technique is not suited, making it difficult in some cases define whether or not a given feature is a grain boundary, low angle grain boundary, or some other feature. The measurements presented here should therefore be treated as useful approximations rather than truly representative data. They cannot be compared with literature grain size values which typically measure only the etched prior austenite boundaries.

Qualitative indications of the homogeneity of microstructure and distribution of precipitates were obtained while performing microscopy. Typically, each sample was investigated for slightly over one hour, mainly in an attempt to get a sense of the microstructure as a whole and to therefore identify a representative area where possible. During these investigations it became clear that the processed LA1 materials were generally more uniform in size and morphology than the starting material. This would be confirmed by later feature size analysis, as 1AR and 1ARHT have a large distribution. Sample #20 also had this large spread in feature size, perhaps due to recrystalization during extrusion because of the imprecise temperature control mentioned previously. Sample #6 did not see homogenization improvement over the 2AR material despite three

passes through the ECAE die. Although feature refinement is reported for all but #20, most of this refinement seems to have occurred in the ferrite regions and, to a lesser extent, by the reduction of lath length rather than width. It makes sense that SPD would preferentially refine the soft phase when both are present.

Although the expected 1-5nm M2X and M6X precipitates are too fine to be discerned in the Jeol 2010 from dislocation clusters, there were some significant differences in the larger M23C6 carbides between starting materials and after processing. The carbides were formed in #20 and #21 most likely because of precipitation during their time in the furnace prior to extrusion although why so many of them formed within grains is unknown. The marginal increase in the number of carbides in the 2AR material after three trips through a 700 C furnace indicate that the carbon content in the material had already precipitated out to the thermodynamic limit before it underwent processing. The clustering of carbides in 2AR and #6 may indicate chemical heterogeneity or simply that the boundaries in some areas were far more energetic/attractive than in others. In any case, the LA2 block must have spent a relatively long time in the 700-900 C region that would encourage M23C6 growth before being sent to Texas A&M.

When comparing the microstructures to literature examples, the 1ARHT group stands out as closer to the ideal overall although only one paper in the literature review showed significant intra-grain carbide formation, and the Mannesmann-sourced T91 in that work otherwise appeared more similar to 2AR and #6 in which ferrite and martensite are more intermixed and there are occasionally ferrite grains that are significantly larger than neighboring grains. Overall, the materials presented here span the range of T91 microstructures well.

Microhardness

There are four factors that significantly impact hardness in T91 that must be kept in mind while analyzing this data: phase composition, grain/feature size, carbides and dislocation density. The martensite phase is much harder than the ferrite and phase transformation dominates hardness in the presented materials. When only one phase is present, refining the microstructure can dramatically harden the material, as seen in the 1AR group. Note that a material with a stronger orientation (and therefore lower angle boundaries) will be weaker than a highly misoriented material with the same feature size. While the large M23C6 carbides have little impact on hardness, a high concentration of fine precipitates can harden the material much like ultrafine precipitation hardened steels. Finally, a dense network of dislocations, which will be formed after SPD, further impedes dislocation motion. With this in mind, we can examine the hardness after processing and heat treatment.

The hardening of the 1AR material with plastic deformation is typical of ECAE processing with grain size refinement and increased dislocation density dominating the changes. However, it was expected that the relatively low extrusion temperature of #1 would result in a higher hardness than the higher temperature, equally strained #4. The sample rod may have upset enough to cause uneven or poor deformation in #1 and unfortunately there was not a large enough sample volume to collect multiple hardness discs. Uneven deformation is quite likely given that the hardness value for #1 is slightly higher than #4 in Peter Hoseman's data (Figure 48).

The softening of 1ARHT and LA2 materials was not expected by the researchers at the time of their extrusion. However, in retrospect the temperatures employed would

have allowed for tempering as described in the literature review and caused the hardening contribution from carbides to decrease as diffusion begins to dissolve them. This tempering was shown to be necessary by the attempted #10 and #18 extrusions. They may have been ductile enough to extrude successfully at 500 C and 600 C had they been tempered beforehand.

Microhardness of bulk materials would traditionally be reported as Vickers. However, an unexpected equipment issue was discovered during the course of this research. The Fischerscope was quite useful in collecting many measurements for each sample but the reported Vickers hardness was significantly different than that measured on a Buehler Micromet II and on a similar machine by collaborators. This stems from the way in which the Fischerscope takes measurements. Traditional Vickers measurements apply a fixed load at a specified rate for a given time. The resulting impression is thereafter measured for D1 and D2 as seen in Figure 56 using a micrometer and crosshairs in the eyepiece and the formula in Figure 56 gives the hardness [86]. This can be aided by or completed automatically with modern computerized systems. In the Fischerscope, the force vs. displacement curve is used along with the known size and shape of the Vickers indenter to calculate the D1 and D2 measurements of the impression left on the sample based on the force vs. displacement curve. However, this procedure assumes an ideal pyramid indent. Deviations from bowing or cracking, such as those in Figure 57, render this calculation inaccurate. It is suspected that this was a factor in the incorrect conversion of hardness values. In many materials, hardness measurements can be sensitive to applied load, distance measurement bias, and other factors. It is therefore important to both report exact measurement technique and use caution with comparing

data taken by different users or on different machines. Because of the large discrepancy in the Fischerscope data, the majority of hardness has been reported here in HIT rather than the Vickers to discourage a direct comparison to other results.

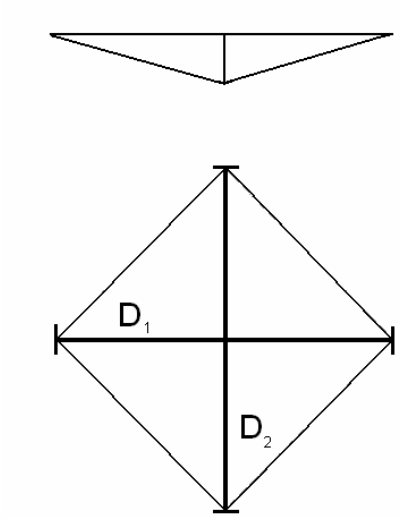

$$H_V = \frac{F}{A} \approx \frac{1.854F}{d^2}. \quad (2)$$

Figure 56. Illustration of Vickers microhardness measurement with equation where F is the indention force, A is the contact area, and d is the average of D1 and D2.

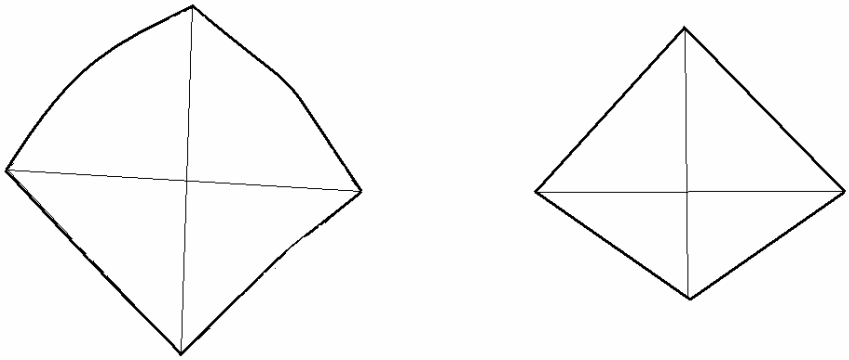

Figure 57. Variations in indent shape.

Tensile Testing

Tensile data for #1-4 could not be obtained due to a lack of material and other processed samples were limited to two coupons each. Unfortunately errors in slicing with the EDM further limited the data to one test in some cases. Given the obvious problems with slipping extensometers illustrated by the data in table 5, the precision of these results can be called into question. Further, the cross-head data and post-test sample measurements indicate that strain is being universally underreported. However, these measurements are far less precise than the extensometer data and simply indicate that some problem might exist. Future measurements will be taken with a different extensometer after evaluation with reference coupons. In any case, the UTS and TE trends should be considered real and there is no cause to call the stress data into question.

The exchange of ductility for ultimate tensile strength is typical for many materials and was expected here. The UTS trends match up well with microhardness values, adding credibility to both. Further improvement might be realized by performing post-processing heat treatments to decrease dislocation concentration and thereby increase ductility without a significant reduction in UTS. The strength increase without ductility penalty seen in #20 over 1AR illustrates the ability of heat treatment and ECAE to improve the mechanical properties of this material.

Sample drift was a problem for SEM imaging of the tensile specimens. Although this was not surprising in the case of samples merely stood on end against carbon tape, drift was still a problem at high magnification for both of the more securely mounted samples. It is assumed that, despite relatively good conduction, there was enough heating in the sample or tape to cause movement of the entire specimen by thermal expansion.

This expansion made EDS difficult and limited the magnification. The lower magnification SEM images show extreme contrast since the digital image acquisition system was not performing well until approximately 100x and higher. However, the important features are easily distinguished.

The 2AR specimens looked as one would expect for brittle materials, with sharp crack propagation lines defining the topology and localized melting at the small scale. The more ductile #6 samples revealed a surprise. The 2-5 um diameter particles and the wells surrounding them seemed to cover the surface. Only a few of these particles were observed in the two 2AR specimens that were examined, although it is unknown if a significant number of particles left the surface upon fracture or subsequent handling especially given the precarious electrostatic hold the particle in Figure 37 seems to have. Initially, the appearances of particles in the #6 specimens lead the investigator to believe that these spheres were a result of phase change during processing. However, since the particle pullout wells are up to tens of microns deep, it is quite possible that there is a comparable concentration of these particles in the LA2 AR material that were not exposed. Collaborators familiar with T91 and similar metals were surprised to see these particles and were unable to venture a guess as to their composition and structure. A literature search was similarly unsuccessful in identifying an explanation. The particles are too large to be the carbides typically reported in this material. They appear undamaged by tensile testing so they are likely harder than the surrounding material. EDS mapping was unsuccessful primarily due to slow sample drift. When focusing on an area dominated by a single particle, Si appeared. The near-perfect spherical shape indicates that the particles were able to coalesce and harden before stress from the

surrounding material could restrict their growth. The particles would therefore likely have a high melting point. SiC particles meet this criterion and the ingredients are in the T91 composition. However, carbon did not show up on EDS and SiC is typically faceted rather than spherical. A Field Emission SEM with a more sophisticated EDS system will be utilized in the future to examine these particles and perhaps give a more definitive answer as to their makeup. A method for collecting enough particles for XRD examination has not been determined.

Heat Treatment

The annealing curves agree well with those in Sikka et. al., although this data starts at 300 C and only goes to the softest point, 800 C. The fact that the hardness drops more significantly in the processed materials than the similarly high hardness 1ARHT can indicate two things. First, the microstructure of the processed material is more homogeneous than the starting material. This agrees with observations during TEM. The other possible factor is that the expected higher concentration of fine precipitates in the untempered 1ARHT is slowing grain growth enough to lead to this difference. It is likely that both mechanisms are in effect and it is unfortunate that limited material prevented a more complete study of #1-4 to help shed light on this issue. Peter Hosemann used most of the material available to him for the heat treatment data shown and did not have remaining material to extend the curve. The optical images from his study reveal prior austenite and subgrain boundaries in most of the material and demonstrate the growth of grain boundaries at 700 C. The curves in his ten hour anneal follow those of the #20 and #21 1 hour anneals over the 0-700 C range. The results of both studies agree with the

typical heat treatment data in the literature with dramatic softening occurring above 700 C.

There is some delay in the softening of 2AR, a further indication of the high concentration of small precipitates in this material which pin the martensite grain boundaries and delay tempering. More generally, this difference in softening point is an illustration of the significant property changes that small chemistry or prior heat treatment changes can induce in ferritic-martensitic steel. The final point of interest in this data is the formation of martensite-dominated steel (and resulting high hardness) despite vacuum cooling. Most sources specify a cooling rate of 4 C/min or better to the martensite start temperature around 400 C in order to transform a significant portion of the material to martensite. It was not expected that this would be achieved in high vacuum surrounded by ceramic but the results clearly indicate the need for furnace cooling from these high temperatures if a martensite-free material is desired.

CHAPTER VI
CONCLUSIONS

The following summarizes the reservations and cautions concerning the data in this work. Feature size has been reported for the materials in this work using TEM images rather than SEM or optical images of etched grain boundaries. This limits the contiguous area from which measurements can be taken. Additionally, there is the difficulty of determining whether a feature is a boundary or not. Further, repeated attempts at producing good micrographs for 1AR failed and the data here is from poor quality samples, as illustrated by Figure 22. Also, the TEM images indicate that #1 has a more misoriented microstructure than #4 and equally refined. Since there does not appear to be a phase difference between the two, it was expected that #1 would be the harder material. Peter Hoseman's data shows this, but data taken at Texas A&M does not. This indicates that there was unequal deformation of the small #1-4 sample rods, especially in the low-temperature #1. A further reservation about the extrusions in general is the reported temperature. As discussed, there is reason to believe that the reported temperature is near the true billet temperature during deformation, however, there will be some variation that must be kept in mind while examining the results. A final reservation concerns the strain data for tensile testing. Given the reported modulus values in Table 5 as well as other indications, there is some concern that the strain data is not as accurate as would be hoped. Despite these reservations, the results provide a base from which to build conclusions.

The following summarizes the findings. Examination of the microstructure reveals that feature size is reduced from ~550nm to ~350nm after processing in most

cases. This is not a great deal of refinement, however, the processed 1AR materials in #1 and #4 have a drastic increase in high angle boundaries, making these small features more like true grains. The increased misorientation of small features is not as prominent, however, in the other materials where martensite is present in significant quantities. The overall affect in the LA1 materials is to make the microstructure more homogeneous even when feature size refinement is less significant. Annealing of as-received, heat treated and processed materials reveals more softening in the extruded material, another indicator of homogeneity. The hardness and ultimate tensile strength increase in this material primarily due to phase transformation from ferrite to martensite and precipitation. Generally, this strengthening comes at the price of ductility as would be expected. However, the case of #20 defies this trend. Here, UTS increases without a drop in ductility. From these findings the following conclusions can be made:

1. Prior heat treatment of ferritic-martensitic steel has a dramatic affect on the capability of ECAE to process it. However, the material can be successfully processed.
2. ECAE coupled with heat treatment can strengthen this material without reducing ductility. In other words, toughness is increased. However, hardness in the more brittle materials is dominated by tempering of the martensite and precipitation.
3. ECAE can impart a modest reduction in average microstructural feature size. This may improve radiation damage tolerance.
4. ECAE can homogenize the microstructure which may benefit corrosion and radiation tolerance.

CHAPTER VII
SUGGESTIONS FOR FUTURE STUDY

One significant area of further study is the simulation of radiation damage in as-received and ECAE processed T91. Originally, high-temperature radiation data was to be obtained by collaborators at Los Alamos. However, due to various factors the experiment was not carried out. Todd Allen at the University of Wisconsin may still demonstrate the effects of ion implantation. Additionally, there is an ongoing long-term experiment at the Paul Scherrer Institute. The ability to simulate neutron damage has recently been re-acquired by Texas A&M University through the rehabilitation of a helium ion beam in the Department of Physics. This can generate implanted material for data on ECAE's effectiveness in reducing radiation damage. The embrittlement and microstructure of the material should be investigated by nanoindentation and cross-sectional TEM. This would be the litmus test for improvement of radiation tolerance damage tolerance in T91 by bulk severe plastic deformation.

Other reactor steels need to be investigated as well. One key investigation is to observe the effectiveness of ECAE on FCC candidates such as 316L. This would advance research in the area by providing a comparison of damage in UFG and nanostructured steels of differing phase types. This might focus future work on the more promising steels.

The investigators believe that a significant decrease in radiation damage will occur if the separation of two dimensional defects such as grain boundaries is 50nm or less. Given that the average grain size of conventional ECAE processed reactor steels is not expected to fall below approximately 200nm, other methods must be considered. The

acquisition of a ball milling machine opens the possibility to use Surface Mechanical Attrition Treatment (SMAT) to refine surface grain size to this level. More conventional use of a ball miller, the breakup of powder to finer size, may be used for an additional proposed grain refinement technique. Powder consolidation of various materials has been carried out using ECAE. Given a starting powder size on the order of 50nm, it may be possible to create a bulk reactor steel sample using this technique. However, this tantalizing possibility has several obstacles and may simply not be possible for nanoscale stainless steel. One additional method that has been widely used to create nanostructured materials is magnetron sputtering. Dr. X. Zhang, a committee member for this thesis, is an expert in magnetron sputtering and is in the process of assembling a system. He has acquired a T91 target and intends to create thin films with it. Although powder consolidation may produce nanostructured reactor steel, SMAT and magnetron sputtering are likely to involve fewer obstacles to 50nm feature size for research. Because of this, it is strongly suggested that these methods be investigated for improving radiation tolerance in reactor steels.

In all cases of future work it is strongly recommended that material be obtained in large quantity from a commercial alloy producer so that many of the frustrating issues that were faced in this work can be avoided.

REFERENCES

[1] B. Constantinescu, C. Sarbu, Luiza Simionescu, Radiat. Phys. Chem. 49 (1997) 411.

[2] N. Igata, A. Kohyama, J. Nucl. Mater. 103 (1981) 409.

[3] F. Chu, M. Song, K. Mitsuishi, H. Yasuda, K. Furuya, J. Electron Microscopy, 51 (2002) S231.

[4] A.E. Hechanova in: Presented at the International Youth Nuclear Congress, Bratislava, Slovakia, April 2000.

[5] H. Sekimoto, S. Makino, K. Nakamura, Y. Kamishima, T. Kawakita, International Seminar on Status and Prospects for Small and Medium Sized Reactors, Cairo, Egypt, 2001, p. 27

[6] I.S. Hwang, S.H. Jeong, B.G. Park, W.S. Yang, K.Y. Suh, C.H. Kim, Prog. Nuc. Energy 37 (2000) 217.

[7] N. Polmar, Guide to the Soviet Navy, Naval Inst. Press, Annapolis, MD 1986 p. 76.

[8] M. Rose, A. G. Balogh, H. Hahn, Nuc. Instr. & Meth. Phys. Research B, 127 (1997) 119.

[9] Y. Chimi, A. Iwase, N. Ishikawa, M. Kobiyama, T. Inami, S. Okuda, J. Nuc. Mater. 297 (2001) 355.

[10] V.M. Segal, Patent of the USSR, No. 575892 1977.

[11] V.M. Segal, Mater. Sci. & Engr. A 197 (1995) 157.

[12] R. Arruffat-Massion, L.S. Tóth, J.-P. Mathieu, Scripta Mat. 54 (2006) 1667.

[13] J-T. Im, K.T. Hartwig, J. Sharp, Acta Mater. 52 (2004) 49.

[14] J.W. Signorelli, P.A. Turner, V. Sordi, M. Ferrante, E.A. Vieira, R.E. Bolmaro, Scripta Mat. 55 (2006) 1099.

[15] R. Lapovok, F.H. Dalla Torre, J. Sandlin, C.H.J. Davies, E.V. Pereloma, P.F. Thomson, Y. Estrin, J. Mech. & Phys. of Solids, 53 (2005) 729.

[16] L.S. Tóth, Comp. Mater. Sci. 32 (2005) 568.

[17] T. Allen, S. Bruemmer, M. Kassner, R. Odette, R. Stoller, G. Was, W. Wolfer, S. Zinkle, J. Elmer, A. Motta, High Temperature Reacter Materials Workshop La Jolla, CA March 2002 p. 74.

[18] R.W. Swindeman, Investigation of Austenitic Alloys for Advanced Heat Recovery and Hot Gas Cleanup Systems, Oak Ridge National Lab, Report OSTI ID: 10177557 TN 1993.

[19] Engr-Tips forum, accessed March 03, 2007 http://www.eng-tips.com/viewthread.cfm?qid=172967&page=1

[20] R.W. Swindeman, M.L. Santella, P.J. Maziasz, B.W. Roberts, K. Coleman, Int. J. Press. Vessels & Piping 81 (2004) 507.

[21] S. Spigarelli, E. Cerri, P. Bianchi, E. Evangelista, Mater. Sci. & Tech. 15 (1999) 1433.

[22] F. Abe in: Presented at the Int. Conf. on Super High Strength Steels, Rome, Italy Nov. 2005.

[23] H. Sakasegawa, T. Hirose, A. Kohyama, Y. Katoh, T. Harada, K. Asakura, T. Kumagai, J. Nuc. Mater 307 (2002) 490.

[24] M.N. Mungole, G. Sahoo, S. Bhargava, R. Balasubramaniam, Mater. Sci. & Engr. A In Press (2007).

[25] M.Taneike, F. Abe, K. Sawada, Nature 424 (2003) 294.

[26] M.L. Santella, R.W. Swindeman, R.W. Reed, J.M. Tanzosh in: Presented at the 6th Int. Conf. on Trends in Welding Research, Pine Mountain, GA, April, 2002.

[27] G. Gupta, Z. Jiao, A.N. Ham, J.T. Busby, G.S. Was, J. Nuc. Mater, 351 (2006) 162.

[28] J. Brozda, M. Zeman, Eng. Failure Anal. 10 (2003) 569.

[29] M.J. Cohn, J.F. Henry, D. Nass, J. Press. Vessel Tech. 127 (2005) 197.

[30] J.F. Henry, Combined Cycle J. 1Q/2005 (2005) 8.

[31] B.E. Farwell, D. Yee, S. Nakazato, 9Cr-1Mo as a Containment Material for the SNAP-8 Boiler, NASA Case Report 72503, Aerojet General Corp. Azusa, CA 1968, p. 1.

[32] V.K. Sikka, C.T. Ward, K.C. Thomas, Ferritic Steels for High Temperature Applications, American Society for Metals, Metals Park, OH 1983. p. 65.

[33] H.E. Chandler, D.F. Baxter, J. Metals Prog. 117 (1980) 24.

[34] L.A. James, Fatigue-Crack Growth Behavior in Ferritic Alloys for Potential GCFR Structural Applications, Report HEDL-TME-80-71, Hanford Engineering Development Lab., Richland, WA

[35] G.S. Barney in: M.S. Davis (Ed), Review of DOE Waste Package Program, U.S. Dept. of Energy Waste Management Dept. Upton, NY, 1983, p. A1-35.

[36] R.L. Klueh, D.S. Gelles, T.A. Lechtenberg, J. Nuc. Mater. 141 (1986) 1081.

[37] R.L. Klueh, in: Proceedings of the Symposium on Materials for Spallation Neutron Sources, The Minerals, Metals, & Materials Society, Orlando, FL 1997, p. 67.

[38] M.H. Mathon, Y. de Carlan, G. Geoffroy, X. Averty, A. Alamo, C.H. de Novion, J. Nuc. Mater. 312 (2003) 236.

[39] F.A. Smidt, Jr., J.R. Hawthorne, V. Provenzano in: Proc. 10th Conf. on Effects of Radiation on Materials, ASTM, Philadelphia, PA 1981 p. 269.

[40] K. Vinzens, H. Laue, B. Hosemann, Nuc. Eng. & Design 119 (1990) 329.

[41] C.S. Jeong, S.Y. Bae, D.H. Ki, K. Watanabe, B.S. Lim, Mater. Sci & Eng. A 449 (2007) 155.

[42] J.J. Sanchez-Hanton , R.C. Thomson, Mater. Sci. & Engr. A In Press (2007).

[43] R.W. Swindeman, V.K. Sikka, P.J. Maziasz in: Presented at the ASME Pressure Vessels and Piping Conf., San Diego, CA, July, 1998.

[44] Elecric Power Research Inst. Combustion Turbine Center website, Accessed March 11, 2007 http://www.eprictcenter.com/infocenter/cc_o_and_m/hrsg/FAQ.php3

[45] Y. Yi, B. Lee, S. Kim, J. Jang, Mater. Sci. & Eng. A 429 (2006) 161.

[46] K. Zabelt, O. Wachter, B. Melzer, VGB Kraftwerkstechnik 76 (1996) 936.

[47] A.P. Greef, C.W. Louw, H.C. Swart, Corrosion Sci. 42 (2000) 1725.

[48] A. Levy, Y.F. Man, Wear 111 (1986) 135.

[49] B.F. Gromov, Y.S. Belomitcev, E.I. Yefimov, M.P. Leonchuk, P.N. Martinov, Y.I. Orlov, D.V. Pankratov, Y.G. Pashkin, G.I. Toshinsky, V.V. Chekunov, B.A. Shmatko, V.S. Stepanov, Nuc. Eng. & Design 173 (1997) 207.

[50] M. Kondo, M. Takahashi, T. Suzuki, K. Ishikawa, K. Hata, S. Qui, H. Sekimoto, J. Nuc. Mater. 343 (2005) 349.

[51] Y. Yamamoto, M.P. Brady, Z.P. Lu, P.J. Maziasz, C.T. Liu, B.A. Pint, K.L. More, H.M. Meyer, E.A. Payzant, Science 316 (2007) 433.

[52] T.R. Allen, L. Tan, G. Gan, G. Gupta, G.S. Was, E.A. Kenik, S. Shutthanandan, S. Thevuthasan, J. Nuc. Mater. 351 (2006) 174.

[53] K. Ono, K. Arakawa, K. Hojou J. Nuc. Mater. 307 (2002) 1507.

[54] F.A. Garner, M.B. Toloczko, J. Nuc. Mater. 206 (1993) 230.

[55] M.B. Toloczko, F.A. Garner, C.R. Eiholzer, J. Nuc. Mater. 212 (1994) 604.

[56] D.S. Gelles, J. Nuc. Mater. 233 (1996) 293.

[57] A. Kumar, F.A. Garner, J. Nuc. Mater. 117 (1983) 234.

[58] F.H. Huang, M.L. Hamilton, J. Nuc. Mater. 187 (1992) 278-293.

[59] Y. Dai, P. Marmy, J. Nuc. Mater. 343 (2005) 247.

[60] G.R. Odette, G.E. Lucas, J. Nuc. Mater. 191 (1992) 50.

[61] E.R. Gilbert, F.A. Garner, J. Nuc. Mater. In Press.

[62] Y. Dai, B. Long, X. Jia, H. Glasbrenner, K. Samec, F. Groeschel, J. Nuc. Mater. 356 (2006) 256.

[63] D. Sapundjiev, A. Al Mazuizi, S. Van Dyck, J. Nuc. Mater. 356 (2006) 229.

[64] B.A. Loomis, J. Nuc. Mater. 141 (1986) 690.

[65] G.S. Was, T. Allen, Mater. Characterization 32 (1994) 239.

[66] P.L. Anderson, F.P. Ford, S.M. Murphy, J.M. Perks in: Proc. of the Fourth Int. Conf. on Environmental Degradation of Materials in Nuclear Power Systems – Water Reactors, Jekyll Island, GA, August, 1989.

[67] V.M. Segal, V.I. Reznikov, A.E. Drobyshevkiy, V.I. Kopylov. Russ Metall 1 (1981) 99.

[68] V.M. Segal, K.T. Hartwig, R.E. Goforth, Mater. Sci. & Eng. A 224 (1997) 107.

[69] V.M. Segal, Mater. Sci. & Eng. A 345 (2003) 36.

[70] S. Li, I.J. Beyerlein, D.J. Alexander, S.C. Vogel, Scripta Mater. 52 (2005) 1099.

[71] Y. Iwahashi, Z. Horita, M. Nemoto, T.G. Langdon, Acta Mater. 46 (1998) 3317.

[72] K. Neishi, Z. Horita, T.G. Langdon, Mater. Sci. & Engr. A 325 (2002) 54.

[73] L.R. Cornwall, K.T. Hartwig, R.E. Goforth, S.L. Semiatin, Mater. Characterization 37 (1996) 295.

[74] I. Karaman, G.G. Yapici, Y.I. Chumlyakov, I.V. Kireeva, Mater. Sci. & Eng. A 410 (2005) 243.

[75] M.A. Gibbs, K.T. Hartwig, L.R. Cornwell, R.E. Goforth, E.A.Payzant, Scripta Mat. 39 (1998) 1699.

[76] S. N. Mathaudhu, K.T. Hartwig, Mater. Sci. & Engr. A 426 (2006) 128.

[77] M. Mabuchi, H. Iwasaki, K. Yanase,K. Higashi, Scripta Mater. 36 (1997) 681.

[78] V.V. Stolyarov, Y.T. Zhu, T.C. Lowe, R.K. Islamgaliev, R.Z. Valiev, Nanostructured Mater. 7 (1999) 947.

[79] J. Robertson, J.T. Im, I. Karaman, K. T. Hartwig, I. E. Anderson, J. Non-Crystalline Solids 317 (2003) 144.

[80] Q. Wei, T. Jiao, S.N. Mathaudhu, E.Ma, K.T. Hartwig, K.T. Ramesh, Mater. Sci. & Eng. A 358 (2003) 266.

[81] B. Wielage, I. Hoyer, S Weis, Welding J. (March 2007) 67.

[82] T.S. Creasy, Y.S. Kang, J. Mater. Proc. Tech. 160 (2005) 90.

[83] P.K. Chaudhury, B. Cherukuri, R. Srinivasan, Mater. Sci. & Engr. A 410 (2005) 316.

[84] S.L. Semiatin, D.P. Delo, Mater. & Design. 21 (2000) 311.

[85] C.Y. Hsu, T.A. Lechtenberg, J. Nuc. Mater. 141 (1986) 1107.

[86] J.H. Westbrook, H. Conrad, The Science of Hardness Testing and Its Research Applications, ASM, Metals Park, OH, 1971. p. 3.

VITA

David Christopher Foley was born and raised in Texas. He split his time between the city and the Texas hill country until enrolling in Trinity University in San Antonio. He received his B.S. in engineering science in May 2005 and went on to Texas A&M University, where he earned his M.S. degree in mechanical engineering in December 2007. He plans to continue graduate studies in pursuit of a Ph.D.

His contact information is:

David Foley

c/o Ted Hartwig

Department of Mechanical Engineering

3123 TAMU

College Station, TX 77843-3123

tdfoley@tamu.edu